Fuel Cell Fundamentals

Chapter 2

Fuel cell fundamentals

Lei Xing[1,*], Jin Xuan[1] and Prodip K. Das[2]

[1]*School of Chemistry and Chemical Engineering, University of Surrey, Guildford, United Kingdom,* [2]*School of Engineering, The University of Edinburgh, Edinburgh, United Kingdom*

Abstract:

Proton exchange membrane fuel cells (PEMFCs) are considered one of the viable solutions to the decarbonization of the transport sector. However, their performance and durability are yet to be competitive with internal engine vehicles due to the complex interaction of electrochemical and physical phenomena in PEMFCs. The electrochemical and physical phenomena that occurred in PEMFCs, including the polarization curves, profiles of the reactant and product species, velocities of species, as well as temperature distribution, could be described by coupling the reaction kinetics with the transport processes of mass, momentum, energy, and charge. In this chapter, the fundamentals and operating principles of PEMFCs are explained along with the governing equations that describe various electrochemical and multi-physics transport processes in PEMFCs.

Keywords: Fuel cell, Reaction kinetics, Transport processes, Two-phase flow, Water management

[*] Corresponding author: L.Xing@surrey.ac.uk

1. Introduction

Fuel cells are electrochemical devices that convert the chemical energy of fuels, e.g., hydrogen or methanol, directly into direct current (DC) electricity. Unlike the traditional internal combustion engine, fuel cells produce electrical energy through an electrochemical reaction, rather than through combustion. A single fuel cell unit consists of a pair of anode and cathode and an electrolyte in between. Individual fuel cells can be connected in series to form a fuel cell stack, which can generate higher power for portable and stationary applications. Depending on different electrolytes, reactants and operating temperatures, fuel cells are mainly categorised into six groups, namely, alkaline fuel cells (AFCs), phosphoric acid fuel cells (PAFCs), molten carbonate fuel cells (MCFCs), solid oxide fuel cells (SOFCs), direct methanol fuel cells (DMFCs), and polymer electrolyte fuel cells (PEFCs). Based on the use of electrolytes, PEFCs are subdivided into two categories*:* proton-exchange-membrane fuel cells (PEMFCs) or anion-exchange-membrane fuel cells (AEMFCs). Among these fuel cells, PEMFCs are best suited for transport and small-scale stationary applications. Thus, great attention has been given to PEMFCs operated with perfluorosulfonic acid (PFSA)-based membranes and hydrogen to combat the increasing global energy consumption and environmental pollution caused by fossil fuel-based internal combustion engines. The electrochemical and physical phenomena that occurred in PEMFCs, including the performance curves, profiles of the reactant and product species, velocities and pressure of reactant gases, as well as the temperature distributions, are determined by the fully coupled electrochemical kinetics and transport of mass and heat. In this chapter, the fundamentals and operating principles, along with governing equations, of PEMFCs are given.

2. Operation principle of proton exchange membrane fuel cells

A typical PEMFC unit consists of a membrane electrode assembly (MEA) sandwiched between the flow field plates of the anode and cathode in which flow channels are machined, as highlighted in Figure 2.1. The MEA includes gas diffusion layer (GDL), microporous layer (MPL), and catalyst layer (CL) at the anode and cathode, respectively, and a proton exchange membrane (PEM) in between. At the anode, hydrogen flows into the anode flow channel and then transports to the CL through the GDL and MPL and then split into protons and electrons in the anode CL (Eq. 2-1). The protons pass through the PEM and reach the cathode CL, while the electrons travel via an external circuit to the cathode. At the same time, air or oxygen flows into the cathode flow channel and then transports to the CL through the GDL and MPL at the cathode. In the cathode CL, oxygen combines with the protons and electrons, which are generated in the anode CL, to produce water (Eq. 2-2).

Anode reaction: $H_2 \rightarrow 2H^+ + 2e^-$ (2-1)

Cathode reaction: $\frac{1}{2}O_2 + 2H^+ + 2e^- \rightarrow H_2O$ (2-2)

Net cell reaction: $H_2 + \frac{1}{2}O_2 \rightarrow H_2O$ (2-3)

The thermodynamic potential for the net cell is calculated by the standard chemical potential at 25°C and 1.0 atm is 1.23 V versus the standard hydrogen electrode (SHE).

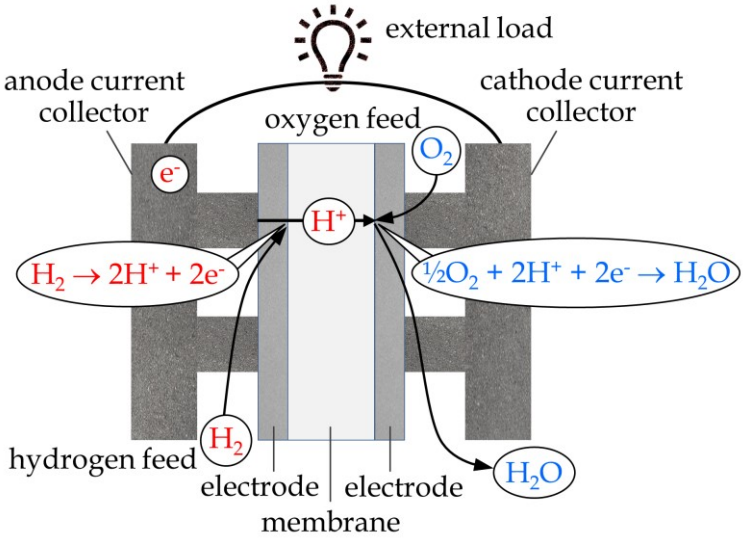

FIGURE 2.1 Schematic diagram and basic operation principle of a proton-exchange membrane fuel cell. Each electrode includes a gas diffusion layer, a microporous layer, and a catalyst layer.

In the case of a fuel cell supplied with reactant gases without a closed electrical circuit, the observed practical cell potential is called the open circuit potential (OCP). The OCP is lower than the theoretical potential due to the activation losses (especially at the cathode) and mixed electrode potential losses in the fuel cell even when no external current is generated [1, 2]. The mixed electrode potential arises due to the unavoidable crossover of fuel through the electrolyte from the anode to the cathode or vice versa. The relationship between fuel cell potential and current density is called the polarisation curve, which is obtained by subtracting the activation polarisation losses, ohmic losses, and concentration polarisation losses from the equilibrium potential. Figure 2.2 shows the polarisation curve and different voltage losses in a typical PEMFC [2, 3]. Note that a majority of the voltage losses occur at the cathode due to the sluggish oxygen reduction reaction (ORR) [4].

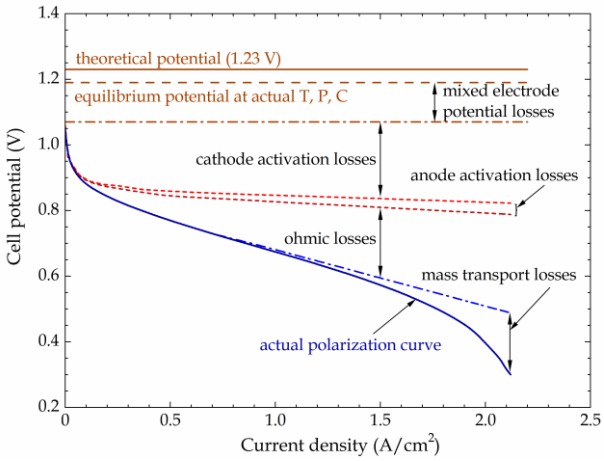

FIGURE 2.2 Voltage losses in a proton-exchange-membrane fuel cell and the resulting polarisation curves.

3. Reaction kinetics and transport processes

3.1 Electrode kinetics

3.1.1 Butler-Volmer kinetics

Fuel cell operation is based on the electrochemical reactions occurring simultaneously at the anode and cathode, which are presented in Eq. (2-1) to Eq. (2-3). The reaction rate of an electrochemical reaction is defined as the speed of the electrochemical reaction proceeds on the electrode surface. Electrical current is generated by the electrons released and consumed in the electrochemical reaction processes. Current density is the current per unit surface area. According to Faraday's law, the current density is proportional to the charge transferred and the consumption of reactants per unit area:

$$i = nFN_i \tag{2-4}$$

where n is the amount of substance, F (96385 C mol^{-1}) is Faraday's constant, N_i (mol m^{-2} s^{-1}) is the flux of reactant per unit area, and i (A m^{-2}) is the current density.

An electrochemical reaction involves either oxidation or reduction of reactant species. Typically, the oxidation process produces electrons while the reduction process consumes the electrons as follows:

$$\mathrm{Rd} \leftrightarrow \mathrm{Ox} + \mathrm{ne}^- \tag{2-5}$$

On an electrode at equilibrium conditions (no external current is generated), both the oxidation and reduction processes occur at equal rates. The net current generated is the difference between the electrons released and consumed:

$$i = nF(k_f c_{Ox} - k_b c_{Rd}) \tag{2-6}$$

where k_f and k_b (s^{-1}) are the forward (reduction) and backward (oxidation) reaction rate coefficients, c_{Ox} and c_{Rd} (mol m^{-2}) are the surface concentrations of the oxidised and reduced

species, respectively. The reaction rate coefficient for an electrochemical reaction is a function of Gibbs free energy.

$$k_{f/b} = \frac{k_B T}{h} \exp\left(\frac{-\Delta G}{R_g T}\right) \tag{2-7}$$

where k_B (1.38×10^{-23} J K^{-1}) is Boltzmann's constant, h (6.626×10^{-34} J s) is the Planck's constant, R_g (8.314 J mol^{-1} K^{-1}) is the universal gas constant, T (K) is the temperature, and ΔG (J mol^{-1}) is the Gibbs free energy, which is considered to consist of both chemical and electrical terms. Consequently, for a reduction reaction:

$$\Delta G = \Delta G_{ch} + \alpha_{Rd} F \phi \tag{2-8}$$

and for an oxidation reaction:

$$\Delta G = \Delta G_{ch} - \alpha_{Ox} F \phi \tag{2-9}$$

where ΔG_{ch} (J mol^{-1}) is the Gibbs free energy of the chemical component, ϕ (V) is the potential, and α_{Rd} and α_{Ox} are the transfer coefficient for reduction and oxidation reactions, respectively. Note that in the case of multi-step electrochemical reactions, $\alpha_{Rd} + \alpha_{Ox}$ is generally equal to n/v, where n is the number of electrons transferred in the overall reaction and v is the stoichiometric number. The forward and backward reaction rate coefficients in Eq. (2-6) are represented, respectively:

$$k_f = k_{0,f} \exp\left(\frac{-\alpha_{Rd} F \varphi}{R_g T}\right) \tag{2-10}$$

$$k_b = k_{0,b} \exp\left(\frac{\alpha_{Ox} F \varphi}{R_g T}\right) \tag{2-11}$$

Therefore, the net current expression is obtained:

$$i = nF\left[k_{0,f} c_{Ox} \exp\left(\frac{-\alpha_{Rd} F \varphi}{R_g T}\right) - k_{0,b} c_{Rd} \exp\left(\frac{\alpha_{Ox} F \varphi}{R_g T}\right)\right] \tag{2-12}$$

At equilibrium, the forward and backward reactions proceed simultaneously, generating zero net currents. In this case, the current densities for both forward and backward reactions are equal.

$$i_0 = nF k_{0,f} c_{Ox} \exp\left(\frac{-\alpha_{Rd} F \varphi_{eq}}{R_g T}\right) = k_{0,b} c_{Rd} \exp\left(\frac{-\alpha_{Ox} F \varphi_{eq}}{R_g T}\right) \tag{2-13}$$

where i_0 (A m^{-2}) is the exchange current density, $k_{0,f}$ and $k_{0,b}$ (s^{-1}) are the reaction rate constant of the forward and backward reaction at standard conditions (25°C and atmospheric pressure), respectively, and φ_{eq} (V) is the equilibrium or reversible potential.

The equilibrium potentials of the hydrogen oxidation reaction (HOR) and the ORR are 0 and 1.229 V at standard conditions. By combing Eq. (2-12) and Eq. (2-13), a relationship between the current density and the overpotential is obtained, which is known as the Butler-Volmer (B-V) equation.

$$i = i_0 \left[\exp\left(\frac{-\alpha_{Rd} F \eta}{R_g T} \right) - \exp\left(\frac{\alpha_{Ox} F \eta}{R_g T} \right) \right] \tag{2-14}$$

where η (V) is the overpotential, defined as the difference between the electrode potential and the equilibrium potential. The B-V equation is valid for both anode and cathode reactions in a PEMFC:

$$i_a = i_{0,a} \left[\exp\left(\frac{-\alpha_{Rd,a} F \eta_a}{R_g T} \right) - \exp\left(\frac{\alpha_{Ox,a} F \eta_a}{R_g T} \right) \right] \tag{2-15}$$

$$i_c = i_{0,c} \left[\exp\left(\frac{-\alpha_{Rd,c} F \eta_c}{R_g T} \right) - \exp\left(\frac{\alpha_{Ox,c} F \eta_c}{R_g T} \right) \right] \tag{2-16}$$

The anode overpotential is positive, which makes the first term in the bracket of Eq. (2-15) negligible and results in a negative sign of the anode current density obtained. Similarly, the cathode overpotential is negative, which makes the second term in the bracket of Eq. (2-16) negligible and leads to a positive sign of the cathode current density.

3.1.2 Agglomerate kinetics

The electrochemical reactions, in which electrons, protons, and gas are involved, only take place on the surface of the catalyst. Reactant gas transports through the micropores within the catalyst layer, electrons travel through the electrically conductive solid, and protons migrate through the electrolyte. According to the functions of the different components within the catalyst layer, the existence of triple-phase boundaries (TPB) is essential, where the content of electrolyte (for proton transfer), void space (for gas transport), and platinum (Pt) dispersed carbon (for catalysis and electron transfer) are interacted, as shown in Figure 2.3.

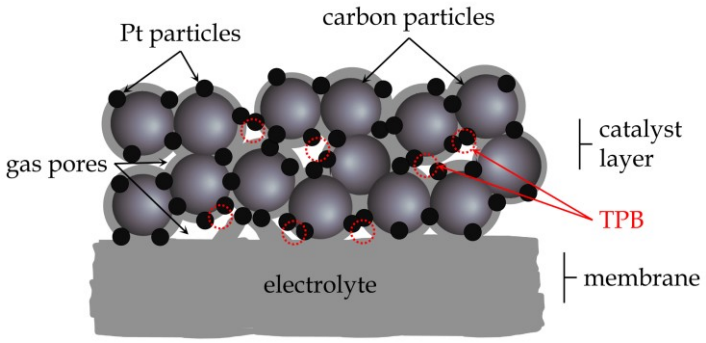

FIGURE 2.3 A simplified schematic diagram of the triple-phase boundary in a catalyst-electrolyte-pores interacted electrode.

A more accurate description of the catalyst layer structure based on the spherical agglomerate model is explained below, where each agglomerate is assumed to consist of three components: platinum dispersed on carbon (Pt/C), ionomer, and void space [5]. The intra-agglomerate void space is defined as the primary pores and the void space between the agglomerate is defined as the secondary pores. As schematically represented in Figure 2.4, the primary pores are partially occupied by ionomer and water and the agglomerates are linked by the ionomer films. When the volume of the produced water exceeds the entire volume of the primary pores, a liquid film is formed surrounding the agglomerates. Reactant gas must dissolve in the ionomer/water film and diffuse through the primary pores before reaching the catalyst particles, which is taken into account in the classic B-V relationship. Thus, agglomerate kinetics is developed to consider the mass transport resistance in addition to electrochemical kinetics.

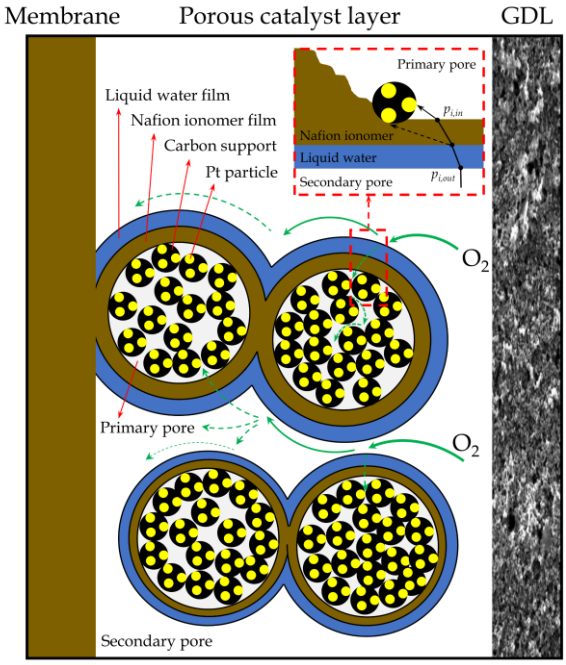

FIGURE 2.4 A schematic illustration of the catalyst layer based on the agglomerate assumption [5]. *Credit: Reprinted from Xing et al., AIChE Journal, 63(11), 4895-4910, 2017, with permission from AIChE.*

Assuming that the concentrations of the dissolved species at the outer and inner boundary of the ionomer/water film are represented by $c_{i,out}$ and $c_{i,in}$ (mol m^{-3}), respectively, the concentration of the dissolved species at the outer interface is described by Henry's law as:

$$c_{i,out} = \frac{p_i}{H_i} \tag{2-17}$$

where p_i (Pa) and H_i (Pa m^3 mol^{-1}) are the partial pressure and Henry's constant of reactant species i, respectively.

The diffusion of reactant through the ionomer/water film can be described by Fick's law:

$$N_i = -D_i^{eff} \frac{\partial c_i}{\partial r} \tag{2-18}$$

where N_i (mol m^{-2} s^{-1}) is the reactants mole flux through the ionomer/water film, D_i^{eff} (m^2 s^{-1}) is the effective diffusion coefficient of reactants, c_i (mol m^{-3}) is the reactant concentration, and r (m) is the radius.

It is assumed that the ionomer/water film is uniformly coated on the agglomerate, and the film thickness is much smaller than the agglomerate. Moreover, the molar rate is conserved in the ionomer/water film, namely the molar rate is constant at the outer boundary of the ionomer/water film. Thus, the reactants mole flux through the ionomer/water film can be derived as

$$C = -(4\pi r^2) D_i^{eff} \frac{\partial c_i}{\partial r} \tag{2-19}$$

with the boundary conditions: $r = r_{agg}, \quad c_i = c_{i,in}$

$$r = r_{agg} + \delta, \quad c_i = c_{i,out} \tag{2-20}$$

where C (mol s^{-1}) is a constant. Integrating Eq. (2-19) and applying the boundary conditions lead to the following expression:

$$C = -D_i^{eff} \left(\frac{c_{i,out} - c_{i,in}}{\delta} \right) 4\pi r_{agg} (r_{agg} + \delta) \tag{2-21}$$

where r_{agg} (m) is the radius of the agglomerate, δ(m) is the thickness of the ionomer/water film. Combing Eq. (2-18), Eq. (2-19) and Eq. (2-21), the reactants mole flux is:

$$N_i = D_i^{eff} \frac{r_{agg}}{(r_{agg} + \delta)} \frac{c_{i,out} - c_{i,in}}{\delta} \tag{2-22}$$

According to mass balance, at a steady state, the amount of the species consumed equals to the species diffusion to the active surface.

$$a_{agg} N_i = R_i \tag{2-23}$$

where a_{agg} (m^{-1}) is the specific area of the agglomerate, defined as the surface area per agglomerate volume, and R_i (mol m^{-3} s^{-1}) is the reaction rate.

Assuming the reactions of either hydrogen oxidation or oxygen reduction as the first-order kinetics with respect to the reactant concentration, we get:

$$R_i = k_{agg} c_i \tag{2-24}$$

where k_{agg} (s^{-1}) is the reaction rate coefficient representing the reactions that occurred in the agglomerate. By introducing the effectiveness factor into Eq. (2-24), the overall reaction rate only depends on the reactant concentration at the outer boundary of the agglomerate, obtained as:

$$R_{i,agg} = E_{agg} k_{agg} c_{i,out} \tag{2-25}$$

where $R_{i,agg}$ (mol m^{-3} s^{-1}) is the reaction rate based on the agglomerate volume and, E_{agg} is the effectiveness factor of the agglomerate, which represents the geometry of the agglomerate and the reactant mass transport resistance within the agglomerate. For the spherical agglomerates, the effectiveness factor is [6]:

$$E_{agg} = \frac{1}{M_{T,agg}} \left[\frac{1}{\tanh(3M_{T,agg})} - \frac{1}{3M_{T,agg}} \right] \tag{2-26}$$

where $M_{T,agg}$ is Thiele's modulus, a dimensionless parameter [6].

$$M_{T,agg} = \frac{r_{agg}}{3} \sqrt{\frac{k_{agg}}{D_{i,agg}^{eff}}} \tag{2-27}$$

where $D_{i,agg}^{eff}$ (m^2 s^{-1}) is the reactant effective diffusion coefficient inside the agglomerate.

According to Faraday's law, the volumetric current density is related to the reactants consumption rate via the following equation:

$$i_{i,agg} = nFE_{agg} k_{agg} c_{i,in} \tag{2-28}$$

$i_{i,agg}$ (A m^{-3}) is the volumetric current density based on the agglomerate volume, and the subscript i refers to anode or cathode, respectively. Combining Eq. (2-22) to Eq. (2-25) the concentration of the dissolved species at the inner boundary of the ionomer/water film is obtained as:

$$c_{i,in} = \left[1 + \frac{E_{agg} k_{agg} (r_{agg} + \delta)\delta}{a_{agg} r_{agg} D_i^{eff}} \right]^{-1} c_{i,out} \tag{2-29}$$

Substituting Eq. (2-29) into Eq. (2-28) gives

$$i_{i,agg} = nF \left[\frac{1}{E_{agg} k_{agg}} + \frac{(r_{agg} + \delta)\delta}{a_{agg} r_{agg} D_i^{eff}} \right]^{-1} c_{i,out} \tag{2-30}$$

According to Henry's law, the above equation becomes

$$i_{i,agg} = nF \frac{p_i}{H_i} \left[\frac{1}{E_{agg} k_{agg}} + \frac{(r_{agg} + \delta)\delta}{a_{agg} r_{agg} D_i^{eff}} \right]^{-1} \tag{2-31}$$

The current density calculated by Eq. (2-14) could transfer to volumetric current density after being corrected by the specific area of the electrode. The agglomerate volumetric current therefore can be related to the Butler-Volmer kinetics as:

$$i_{i,agg} = a_{agg} i_0 \left[\exp\left(\frac{-\alpha_{Rd} F\eta}{RT} \right) - \exp\left(\frac{\alpha_{Ox} F\eta}{RT} \right) \right] \tag{2-32}$$

On the inner boundary of the agglomerate, the intrinsic volumetric current density is obtained as:

$$i_{i,agg} = nFk_{agg}c_{i,in} \tag{2-33}$$

Comparing the above two expressions, the reaction rate is obtained as:

$$k_{agg} = \frac{a_{agg}i_0}{nFc_{i,in}}\left[\exp\left(\frac{-\alpha_{Rd}F\eta}{RT}\right) - \exp\left(\frac{\alpha_{Ox}F\eta}{RT}\right)\right] \tag{2-34}$$

3.1.3 Conservation of charge

Assuming a finite volume dV (m^3) carries an amount of charge dG_v (C), the charge density g_v (C m^{-3}) is:

$$g_v = \frac{dG_v}{dV} \tag{2-35}$$

where the total charge of the volume V is:

$$\int dG_v = \int dVg_v \tag{2-36}$$

The change of total charge in time generates current flow in and/or out of the surface dS (m^2) surrounding the volume dV. The expression of conservation of charge is, therefore:

$$\frac{d}{dt}\int dVg_v = -\oint dS \cdot \mathbf{i} \tag{2-37}$$

where $\mathbf{i}$ (A m^{-2}) is the current density vector. By using the Gauss divergence theorem and assuming that the volume V did not change with time, the above equation can be rewritten as

$$\frac{d}{dt}\int dVg_v = -\nabla \cdot \mathbf{i} \tag{2-38}$$

Assuming the charge density at any location does not change with time and adding a source term Q_i (A m^{-3}) leads to

$$\nabla \cdot \mathbf{i} = Q_i \tag{2-39}$$

If no external source is applied, Q_i is equal to the volume current density i_v (A m^{-3}). The current density vector $\mathbf{i}$ can be related to the electric filed $\mathbf{E}$ (V m^{-1}) and conductivity σ (S m^{-1}) by Ohm's law as:

$$\mathbf{i} = \sigma \cdot \mathbf{E} \tag{2-40}$$

At a specific point within the electric field, the voltage is equal to the negative gradient of the potential, thus

$$\mathbf{E} = -\nabla\phi \tag{2-41}$$

Substituting Eq. (2-40) and Eq. (2-41) into Eq. (2-39) gives

$$\nabla \cdot \mathbf{i} = \nabla(-\sigma\nabla\phi) = Q_i \tag{2-42}$$

Applying Eq. (2-42) on the solid (electrode) and electrolyte (membrane and ionomer) phases, respectively, two sub-equations are obtained [7]:

$$\nabla \cdot \mathbf{i}_s = \nabla(-\sigma_s^{eff} \nabla \varphi_s) = Q_s \tag{2-43}$$

$$\nabla \cdot \mathbf{i}_M = \nabla(-\sigma_M^{eff} \nabla \varphi_M) = Q_M \tag{2-44}$$

where σ_s^{eff} and σ_M^{eff} (S m^{-1}) are the effective electrical conductivity for the solid phase and electrolyte conductivity for the membrane and ionomer, respectively. For any volume of the computational domain, the electronic and the ionic currents generated are equal, leading to:

$$\nabla \cdot \mathbf{i}_s + \nabla \cdot \mathbf{i}_M = 0 \tag{2-45}$$

In a porous media, the source terms Q_s and Q_M can be expressed in terms of the volumetric current for the electrode and electrolyte, respectively. The total current generated in the anode must be equal to the total current consumed in the cathode. In the situation of no external resource the conservation of charge requires that:

$$Q_s = -Q_M \tag{2-46}$$

$$\int_{V_{CL,a}} i_a dV = -\int_{V_{CL,c}} i_c dV \tag{2-47}$$

The average volumetric current density i_{avg} (A m^{-3}) is expressed as:

$$i_{avg} = \frac{1}{V_{CL,a}} \int_{V_{CL,a}} i_a dV = -\frac{1}{V_{CL,c}} \int_{V_{CL,c}} i_c dV \tag{2-48}$$

where $V_{CL,a}$ and $V_{CL,c}$ (m^3) are the volume of the catalyst layer of anode and cathode, respectively. The surface overpotential, the driving force for the transfer current density in an electrochemical reaction, is defined as [8]:

$$\eta = \phi_s - \phi_M - E^{eq} \tag{2-49}$$

where E^{eq} (V) is the equilibrium potential, which is zero on the cathode and is equal to the theoretical cell potential at a given temperature and pressure on the cathode side calculated by the Nernst equation. The equilibrium potential for the hydrogen-based anode is zero and the following simplified expression could be used for the calculation of the equilibrium potential of the cathode [8-10]:

$$E_c^{eq} = 1.482 - 8.45 \times 10^{-4} T + 4.31 \times 10^{-5} T \ln(p_{H_2} p_{O_2}^{0.5}) \tag{2-50}$$

3.1.4 Exchange current density and charge transfer coefficient

Exchange current density and charge transfer coefficient are the two most important parameters in Butler-Volmer to determine the intrinsic activity of the electrochemical catalysts. Exchange current density is the current densities for the anode and cathode when both the forward and

backward reactions are equal. It is analogous to the rate constant in chemical reactions and is a function of the operating temperature and partial pressure of the reactant. The exchange current density can be expressed as [8]:

$$i_0 = i_0^{ref} a_{CL} \left(\frac{p_r}{p_r^{ref}} \right)^{\gamma} \exp\left[-\frac{E}{RT}\left(1 - \frac{T}{T^{ref}}\right)\right] \tag{2-51}$$

where i_0^{ref} (A m^{-2}) is the reference exchange current density per unit catalyst surface area obtained at the reference temperature of 25°C and pressure of 1.0 atm, a_{CL} (m^{-1}) is the specific area of the catalyst layer, p_r (kPa) is the reactant partial pressure, p_r^{ref} (kPa) is the reference pressure, γ (0.5 for hydrogen oxidation reaction and 1.0 for oxygen reduction reaction [11-13]) is the pressure dependency coefficient, T^{ref} (298 K) is the reference temperature, E (kJ mol^{-1}) is the activation energy, it is found to be 72.4 kJ mol^{-1} for oxygen reduction on cathode [14], and 16.9 kJ mol^{-1} for hydrogen oxidation on anode [12], respectively.

Exchange current density is a reflection of the activity of the surface of the electrode. Higher exchange current density means a lower energy barrier that the charge must overcome in moving from the electrolyte to the catalyst surface. In a PEMFC, the exchange current density of the anode is several orders of magnitude larger than that of the cathode. In other words, more current is generated at a fixed overpotential with a higher exchange current density, and the cathode overpotential is much larger than the anode overpotential. For this reason, the polarisation curve is mainly determined by the ORR at the cathode. According to the literature [4, 15, 16], the reference exchange current density (i_0^{ref}) for the anode is 1.0 A cm^{-2} whereas it is much smaller for the cathode and is a function of temperature:

$$i_0^{ref} = 10^{\left(3.507 - \frac{4001}{T}\right)} \tag{2-52}$$

The transfer coefficients account for the electrical effects on the change of Gibbs free energy in an electrochemical reaction. Since the forward and backward reactions co-exist in the oxidation reaction at the anode and the reduction reaction at the cathode. Sousa et al. [17] assumed that the transfer coefficient for the reduction reaction, α_{Rd}, is equal to the transfer coefficient for the oxidation reaction, α_{Ox} , for both anode and cathode, leading to $\alpha_{Rd,a} = \alpha_{Ox,a} = \alpha_a$ and $\alpha_{Rd,c} = \alpha_{Ox,c} = \alpha_c$. According to Sun et al. [6], $\alpha_{Rd} + \alpha_{Ox}$ is set to unity. For oxygen reduction reaction on cathode: $\alpha_{Rd,c} = \alpha_c$, $\alpha_{Ox,c} = 1 - \alpha_c$; for hydrogen oxidation reaction on anode: $\alpha_{Ox,a} = \alpha_a$, $\alpha_{Rd,a} = 1 - \alpha_a$.

It is well known that the transfer coefficient has a significant influence on the current density. However, it is difficult to predict the accurate value of the transfer coefficient for a particular system as it is a function of numerous conditions, such as temperature, pressure, catalyst

structure, and reactant impurity. Parthasarathy et al. [18] found two different Tafel slopes in different ranges of cell voltages, that is lower at higher cell voltages and higher at lower cell voltages. Based on their experimental measurement, the cathode transfer coefficient was regressed by Sun et al. [6] as:

$$\alpha_c = 0.495 + 2.3\times10^{-3}(T - 300) \tag{2-53}$$

In comparison with the cathode transfer coefficient, the anode transfer coefficient changes slightly as the operating condition changes. Therefore, the value reported by Bernardi and Verbrugge [4] of $\alpha_a = 0.5$ is typically used.

With the development of advanced Pt-based materials, the activity of electrochemical catalysts has been significantly improved. Thus, the expressions of exchange current density and charge transfer coefficient developed in the 2000s are not suitable for state-of-the-art catalysts. However, the methodologies as described in the work of Parthasarathy et al. [18] are still valid, in which the Tafel slope was derived through the simplification of the Butler-Volmer equation. For the oxygen reduction reaction at the cathode, the second term in the bracket of the B-V equation could be omitted due to its very small value. After a rearrangement, Eq. (2-16) becomes

$$\eta_c = \frac{R_g T}{\alpha_c F}\ln i_0 - \frac{R_g T}{\alpha_c F}\ln i \tag{2-54}$$

Substituting Eq. (2-49) into the above equation leads to

$$\varphi_s - \varphi_M - E^{eq} = \frac{R_g T}{\alpha_c F}\ln i_0 - \frac{R_g T}{\alpha_c F}\ln i \tag{2-55}$$

In the electrochemical control zone at high cell voltage, the electrolyte phase potential, φ_M, is negligibly small and the solid phase potential, φ_s, is approximately equal to the cell voltage *E*. Thus, Eq. (2-55) could be expressed as:

$$E - E^{eq} = \frac{R_g T}{\alpha_c F}\ln i_0 - \frac{R_g T}{\alpha_c F}\ln i \tag{2-56}$$

Plotting *E* as a function of $\ln i$ gives a straight line with a slope of $R_g T/\alpha_c F$ and an intercept of $(R_g T/\alpha_c F)\ln i_0$, then the exchange current density, i_0, and charge transfer coefficient, α_c, are obtained.

3.1.5 Electrical and ionic conductivities

The electrical conductivities of GDL and CL are different owing to the different compositions of the two domains and depend on the composition, e.g., the volume fractions of the components responsible for the conductivity. Therefore, appropriate corrections are essential. The most widely used approximation for effective electrical conductivities is the Bruggeman approximation. However, there are many correlations beyond the Bruggeman approximation available in the open literature for effective electrical conductivities [19]. For instance, The effective electronic conductivity for the CL can be obtained using the following correlation [20]:

$$\sigma_s^{eff} = \sigma_s \frac{2-2\varepsilon_e}{\varepsilon_e + 2} \tag{2-57}$$

where σ_s (S m^{-1}) is the electrical conductivity of the solid phase (platinum dispersed carbon in the catalyst layer), ε_e is the volume fraction of the non-conductor materials, e.g., ionomer and void space in the CL. The electronic conductivity of Vulcan XC-72 carbon black is 450 S m^{-1} [21] and the electrical conductivity of platinum is regressed from the experimental data as [22]:

$$\sigma_{Pt} = 1.7209 \times 10^9 T^{(-0.9259)} \tag{2-58}$$

Proton transport between agglomerates requires sufficiently thick ionomer films surrounding agglomerates because the contact between agglomerates decreases when ionomer thickness decreases, which leads to a decrease in proton transport. The effective ionic conductivity of CL, σ_M^{eff} (S m^{-1}), can be obtained using the following equation [23]:

$$\sigma_M^{eff} = (1-\varepsilon_{CL})\left[1 + \frac{(\varepsilon_{agg,M} - 1)}{(1 + \delta_M / r_{agg} + a_0)^3}\right]\sigma_M \tag{2-59}$$

where $\varepsilon_{agg,M}$ is the volume fraction of the ionomer in agglomerate, δ_M (m) is the thickness of the ionomer film, r_{agg} (m) is the radius of the agglomerate. The values of the parameters of $\varepsilon_{agg,M}$, δ_M and r_{agg} are associated with the CL structure. Note that the above expression is developed by improving the equation of Jaouen et al. [24, 25]. To capture the trend of the relationship between δ_M and σ_M^{eff} ($\delta_M \to 0, \sigma_M^{eff} \to 0$), the dimensionless parameter a_0 is added, which is given by:

$$a_0 = \min\left[0, \left(\frac{\delta_M}{r_{agg}} + \sqrt[3]{(1-\varepsilon_{agg,M})} - 1\right)\right] \tag{2-60}$$

The intrinsic ionic conductivity, σ_M (S m^{-1}), strongly depends on temperature and water content, which can be obtained from [28].

$$\sigma_M = \exp\left[1268\left(\frac{1}{303}-\frac{1}{T}\right)\right](0.5139\lambda - 0.326) \tag{2-61}$$

where λ is the membrane water content.

3.2 Multicomponent mass transport

3.2.1 Conservation of momentum

The velocity and pressure of reactant gases flowing through the channel and porous media could be known by solving the conservation equation of momentum. The momentum flow through the volume element can be described by two mechanisms: convection and diffusion. Considering the fluid flows through all faces of the volume element, the conservation of momentum can be written as [26]:

$$\frac{\partial(\rho\mathbf{u})}{\partial t} = -\nabla\cdot(\rho\mathbf{uu}) - \nabla\cdot p - \nabla\cdot\boldsymbol{\tau} + \rho\mathbf{g} \tag{2-62}$$

where ∇p (Pa m^{-1}) is the pressure gradient, $\boldsymbol{\tau}$ (kg m^{-1} s^{-2}) is the shear stress tensor, and $\mathbf{g}$ (m s^{-2}) is the gravitational acceleration vector.

The term on the left-hand side of Eq. (2-62) means the rate of momentum increase per unit of volume while on the right-hand side the first term is the rate of momentum gain by convection per unit of volume, the second term is the pressure force on element per unit of volume, the third term describes the rate of momentum gain by viscous transfer per unit of volume, and the last term is the gravitational force on the element per unit of volume. This equation, which is valid for any continuous medium, is the general form of the motion equation. If the behaviour of the fluids obeys Newton's law of viscosity, in which the shear force per unit of area is proportional to the negative of the local velocity gradient, the shear stress tensor is therefore being expressed as [26]:

$$\boldsymbol{\tau} = \mu\left[\nabla\mathbf{u} + (\nabla\mathbf{u})^T - \frac{2}{3}(\nabla\cdot\mathbf{u})\mathbf{I}\right] \tag{2-63}$$

where $\mathbf{I}$ is the identity matrix.

To describe the momentum balance in the porous media, the Brinkman equation [27] is normally used. This equation was developed based on Darcy's law by Brinkman in 1949. An additional term was added to Darcy's law accounting for the viscous transport in the momentum balance. And both the pressure and flow velocity vector were treated as independent variables in the Brinkman equation shown as follows:

$$\left(\frac{\rho}{\varepsilon}\right)\frac{\partial\mathbf{u}}{\partial t} = -\mathbf{u}\frac{\mu^{eff}}{K} - \nabla\cdot p - \nabla\cdot\boldsymbol{\tau} + \rho\mathbf{g} \tag{2-64}$$

where K (m^2) and ε are the permeability and porosity of the porous media, respectively, and μ^{eff} (Pa s) is the effective viscosity of the fluid. The shear stress tensor is similar to that in Eq. (2-63) but the porosity of the porous media is included:

$$\boldsymbol{\tau} = \frac{\mu}{\varepsilon}[\nabla \mathbf{u} + (\nabla \mathbf{u})^T - \frac{2}{3}(\nabla \cdot \mathbf{u})\mathbf{I}] \tag{2-65}$$

For a multi-component mixture, the motion equation is very similar to the equations developed for a single fluid. The difference is that the last term, $\rho \mathbf{g}$ is replaced by $\sum \rho_i \mathbf{g}_i$, which accounts for the fact that each species may be affected by different external force per unit of mass. Simultaneously, a unit tensor $\boldsymbol{\delta}$ is introduced to the pressure term shown as follows:

$$\frac{\partial(\rho \mathbf{u})}{\partial t} = -\nabla \cdot (\rho \mathbf{u}\mathbf{u}) - \nabla \cdot (p\boldsymbol{\delta}) - \nabla \cdot \boldsymbol{\tau} + \sum_{i=1}^{n} \rho_i \mathbf{g}_i, \qquad i = 1,2,3,.....,n \tag{2-66}$$

$$\left(\frac{\rho}{\varepsilon}\right)\frac{\partial \mathbf{u}}{\partial t} = -\mathbf{u}\frac{\mu^{eff}}{K} - \nabla \cdot (p\boldsymbol{\delta}) - \nabla \cdot \boldsymbol{\tau} + \sum_{i=1}^{n} \rho_i \mathbf{g}_i, \qquad i = 1,2,3,.....,n \tag{2-67}$$

Note that the flow velocity in equations from Eq. (2-62) to Eq. (2-67) is the superficial averaged velocity, which is defined as the volume rate of flow through a unit cross-sectional area including both pores and solid matrix. This definition makes the velocity field continuous across the boundaries between the porous and free flow regions. The flow therefore can be described by the same velocity in the entire domain.

3.2.2 Maxwell-Stefan diffusion

The multi-component mass transport of gaseous reactant mixture within the porous electrode is described by the Maxwell-Stefan equation as

$$\rho^g \mathbf{u}^g \cdot \nabla w_i^g - \nabla \cdot \left[-\rho^g \sum_{j=1}^{N} (1-s) D_{ij} (\nabla x_j^g - w_j^g) \frac{\nabla p}{p} + D_i^T \frac{\nabla T}{T} \right] = M_i S_i^g \tag{2-68}$$

where w_i^g, w_j^g and M_i (kg mol^{-1}) are the mass fraction, mole fraction and molecular weight of species *i*, respectively. D_{ij} (m^2 s^{-1}) and D_i^T (m^2 s^{-1}) are the binary diffusion coefficient and the thermal diffusion coefficient, respectively, T (K) is the temperature, S_i^g (mol m^{-3} s^{-1}) is the source terms, which account for the electrochemical reactions taking place within the porous catalyst layer shown as follow:

$$S_{H_2}^g = \frac{i_a}{2F}, \; S_{O_2}^g = -\frac{i_c}{4F}, \; S_w^g = \frac{i_c}{2F} \tag{2-69}$$

Note that ρ^g (kg m^{-3}) is the density of the gas mixture, which is given by the ideal gas law:

$$\rho^g = \frac{p^g M_n}{RT} \tag{2-70}$$

where p^g (Pa) is the pressure of the gas mixture and M_n (kg mol^{-1}) is the mean molecular weight of the gas mixture, which can be related to the mole fraction of the component as follow:

$$M_n = \sum_{i=1}^{n} x_i M_i \tag{2-71}$$

where *n* is the number of component gas in the gas mixture and, M_i (kg mol^{-1}) is the molecular weight of the species *i*.

According to the agglomerate assumption, reactant gases must first transport through the secondary pores to the outer boundary of the ionomer films surrounding the agglomerate, then diffuse into the primary pores inside the agglomerate and reach the active sites for electrochemical reaction. Note that ionomer and water are also the diffusive media of gas transport, but with a few orders of magnitude lower diffusivity in comparison with the void space. Neglecting the mass transport of gas species through ionomer and water, the effective diffusion coefficient of species *i* through the secondary pores can be approximated using the Bruggman relationship as [15, 28-30]

$$D_{i,s}^{eff} = \varepsilon_s^{1.5} D_{i-P}^0 \tag{2-72}$$

where ε_s is the volume fraction of secondary pores, D_{i-P}^0 (m^2 s^{-1}) is the equivalent diffusion coefficient of species *i* in void space.

When reactant gases diffuse through the ionomer film, they must transport through the primary pores inside the agglomerates to the surface of the platinum particles. The agglomerates consist of four components namely, Pt/C, ionomer, water and primary pores. Assuming primary pores are the gas transport media, the effective transport coefficient of gas species *i* within the agglomerates is:

$$D_{i,p}^{eff} = \varepsilon_{agg,p}^{1.5} D_{i-P}^0 \tag{2-73}$$

in which $\varepsilon_{agg,p}$ is the volume fractions of primary pores within the agglomerate.

By taking the Knudsen diffusion into account, the equivalent diffusion coefficient of species *i* in void space, D_{i-P}^0 (m^2 s^{-1}), is:

$$\frac{1}{D_{i-P}^0} = \frac{1}{D_{i-g}^0} + \frac{1}{D_{Kn,i}} \tag{2-74}$$

where D_{i-g}^{0} (m^2 s^{-1}) is the intrinsic diffusion coefficient, and $D_{Kn,i}$ (m^2 s^{-1}) is the Knudsen diffusion coefficient of species *i*.

$$D_{i-g}^{0} = \frac{1-x_i}{\sum_{j\neq i}(x_j / D_{ij}^{0})} \tag{2-75}$$

where D_{ij}^{0} (m^2 s^{-1}) is the binary diffusion coefficient of species *i* and *j*, which is calculated by the equation developed by Bird et al. [26]:

$$D_{ij}^{0} = 1.8583\times10^{-7}\sqrt{T^3(\frac{1}{M_i}+\frac{1}{M_j})}\frac{1}{p\sigma_{ij}^{2}\Omega_{ij}} \tag{2-76}$$

where,

$$\sigma_{ij} = \frac{1}{2}(\sigma_i+\sigma_j),\ \varepsilon_{ij} = \sqrt{\varepsilon_i\varepsilon_j} \tag{2-77}$$

Ω_i and Ω_{ij} are functions of the reduced temperature T_i^* and T_{ij}^*.

$$T_i^* = \frac{\kappa}{\varepsilon_i}T,\ T_{ij}^* = \frac{\kappa}{\varepsilon_{ij}}T \tag{2-78}$$

There are empirical expressions for calculating Ω_i and Ω_{ij} written as:

$$\Omega_i = A/(T_i^*)^B + C/\exp(T_i^*D) + E/\exp(T_i^*F) \tag{2-79}$$

$$\Omega_{ij} = A/(T_{ij}^*)^B + C/\exp(T_{ij}^*D) + E/\exp(T_{ij}^*F) + G/\exp(T_{ij}^*H) \tag{2-80}$$

The Lennard-Jones potential parameters are listed in Table 2.1.

Table 2.1 Lennard-Jones potential parameters [26].

Species *i*	M_i	σ_i	ε_i/κ
H_2	2.016	2.915	38.0
O_2	32.000	3.433	113.0
N_2	28.013	3.667	99.8
H_2O	18.000	2.641	809.1

Ω_i	A=1.16145; B=0.14874; C=0.52487; D=0.77320; E=2.16178; F=2.43787
$\Omega_{i,j}$	A=1.06036; B=0.15610; C=0.19300; D=0.47635; E=1.03587; F=1.52996; G=1.76474; H=3.89411

The temperature-dependent binary diffusion coefficients for all pairs of gas species at 1.0 atm are presented in Figure 2.5.

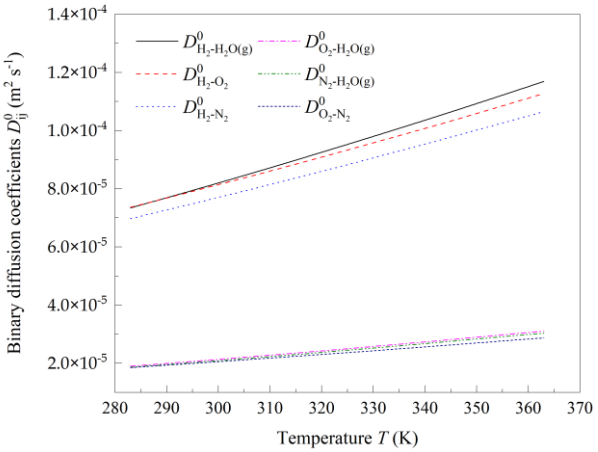

FIGURE 2.5 Temperature-dependent binary diffusion coefficients of gas species pairs at 1.0 atm [31].

3.2.3 Knudsen diffusion

Knudsen diffusion is a means of diffusion that occurs when the scale length of a system is comparable to or smaller than the mean free path of the particles involved. Knudsen's effect on reactant gas diffusion should be considered when the Knudsen number (K_n) is greater than 0.1 [24, 25]. The Knudsen number and Knudsen diffusion coefficient of oxygen diffusion in porous media are [10, 32]:

$$K_n = \frac{k_B T}{\sqrt{2}\pi p \sigma_{ii} d_{avg}} \tag{2-81}$$

$$D_{K_n,i} = \frac{d_{avg}}{3}\sqrt{\frac{8RT}{\pi M_i}} \tag{2-82}$$

where k_B (1.38065×10^{-23} J K^{-1}) is the Boltzmann constant, σ_{ii} (m) is the particle diameter, and d_{avg} (m) is the average pore diameter in the catalyst layer, which can be calculated as [10, 32]:

$$d_{avg} = \frac{4}{3}\frac{\varepsilon_{CL}}{1-\varepsilon_{CL}} r_{agg} \tag{2-83}$$

where ε_{CL} and r_{agg} (m) are the porosity of the catalyst layer and the radius of the agglomerate, respectively.

Taking the effective diffusion coefficient of oxygen through the void space of porous electrode as an example, as shown in Figure 2.6, the Knudsen effect is significant (particularly at higher temperatures).

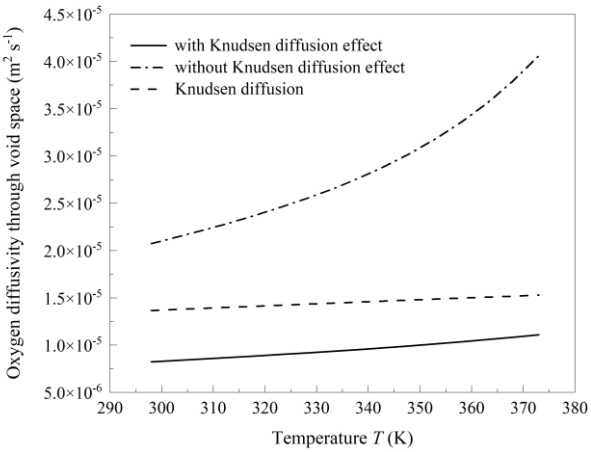

FIGURE 2.6 Effective oxygen diffusion coefficient through void space of porous electrode [31].

The thermal diffusion coefficient of species *i* in the gas mixture, D_i^T ($m^2\ s^{-1}$), can be expressed as the quotient of the thermal conductivity and specific heat capacity as:

$$D_i^T = M_i k_i / c_{p,i} \tag{2-84}$$

The thermal diffusion of gas species is normally omitted in most research owing to the limited influence on the overall diffusivity compared to that trigged by the concentration gradient.

3.3 Heat transport

3.3.1 Conservation of energy

The equation of energy for a multi-component mixture is given by using the methodology developed by Bird et al. [26]:

$$\rho\left(\frac{\partial U}{\partial t} + \mathbf{u}\cdot\nabla U\right) = -\nabla\cdot\mathbf{q} - p\nabla\cdot\mathbf{u} - \boldsymbol{\tau}\nabla\cdot\mathbf{u} + Q_e \tag{2-85}$$

The term on the left-hand side of the equation above represents the rate of internal energy gained per unit of volume, the first term on the right hand is the rate of internal energy input per unit of volume by conduction, the second term on the right hand is the reversible rate of internal energy increase per unit of volume by compression, the third term on the right hand is

the irreversible rate of internal energy increase per unit of volume by viscous dissipation and Q_e is the heat source.

Instead of internal energy, the above expression can be written in terms of the temperature and heat capacity of the fluid, which becomes more convenient for calculating the temperature profiles. At constant pressure, the internal energy can be related to the temperature and heat capacity via the following equation:

$$\frac{\partial U}{\partial t} = -p\frac{\partial V}{\partial t} + c_p \frac{\partial T}{\partial t} \tag{2-86}$$

where V (m^3 kg^{-1}) is the volume per unit of mass, and c_p (J mol^{-1} K^{-1}) is the averaged heat capacity of the multi-component mixture at constant pressure, which can be calculated by the heat capacity and mole fraction of the species of the multi-component mixture:

$$c_p = \sum_{i=1}^{n} c_{p,i} x_i \ , \ i = 1,2,3,.....,n \tag{2-87}$$

With the aid of the equation of continuity $\rho(dV/dt) = \nabla \cdot \mathbf{v}$, then multiplying both sides of Eq. (2-86) by the averaged density of the multi-component mixture and combing Eq. (2-85) gives:

$$\rho c_p \frac{\partial T}{\partial t} + \rho c_p \mathbf{u} \cdot \nabla T = -\nabla \cdot \mathbf{q} - \boldsymbol{\tau} \nabla \cdot \mathbf{u} + Q_e \tag{2-88}$$

The term $\boldsymbol{\tau} \nabla \cdot \mathbf{u}$ is only significant in a high-speed flow system in which the velocity gradient is large and negligible for PEFMCs. By substituting $\mathbf{q} = -k\nabla T$ into the above equation, a second-order partial differential equation for temperature profiles can be written as:

$$\rho c_p \frac{\partial T}{\partial t} + \rho c_p \mathbf{u} \cdot \nabla T - \nabla \cdot (k \nabla T) = Q_e \tag{2-89}$$

For a multi-phase heat transfer process occurred in the porous media, Eq. (2-89) becomes:

$$\frac{\partial}{\partial t}[\sum_{i=g,l,s} (\varepsilon \rho_i c_{p,i}) T] + \nabla \cdot [\sum_{i=g,l} (\varepsilon \rho_i c_{p,i} \mathbf{u}_i) T] - \nabla \cdot (\sum_{i=g,l,s} k_i \nabla T) = Q_e \tag{2-90}$$

where ε is the porosity, the subscripts *g*, *l*, and *s* refer to phases of gas, liquid and solid, respectively.

3.3.2 Specific heat capacity and thermal conductivity

The specific heat capacity and the thermal conductivity of the gas mixture are obtained by using an empirical equation developed by Wike [33],

$$c_p^g = \sum_i x_i c_{p,i}^g, \quad k^g = \sum_i \frac{x_i k_i}{\sum_j x_j \Phi_{ij}} \tag{2-91}$$

in which

$$\Phi_{ij} = \frac{1}{\sqrt{8}}\left(1+\frac{M_i}{M_j}\right)^{-0.5}\left[1+\left(\frac{k_i}{k_j}\right)^{0.5}\left(\frac{M_j}{M_i}\right)^{0.25}\right]^2, \quad \Phi_{ji} = \frac{k_j}{k_i}\frac{M_i}{M_j}\Phi_{ij} \tag{2-92}$$

where c_p^g (J mol^{-1} K^{-1}) is the specific heat capacity of the gas mixture, x_i is the mole fraction of species *i* in gas mixture, $c_{p,i}^g$ (J mol^{-1} K^{-1}) is the specific heat capacity of species *i* in gas mixture, k^g (W m^{-1} K^{-1}) is the thermal conductivity of the gas mixture, k_i (W m^{-1} K^{-1}) is the thermal conductivity of species *i* in gas mixture, M_i (kg mol^{-1}) is the molecular weight of species *i*.

The expressions for the specific heat capacities of each gas component including hydrogen, oxygen, nitrogen and water vapour are:

$$c_{p,H_2}^g = 1.914\times10^{-6}T^2 - 8.314\times10^{-4}T + 28.890 \tag{2-93}$$

$$c_{p,O_2}^g = -4.281\times10^{-6}T^2 + 1.371\times10^{-2}T + 25.431 \tag{2-94}$$

$$c_{p,N_2}^g = 1.788\times10^{-5}T^2 + 2.924\times10^{-3}T + 27.848 \tag{2-95}$$

$$c_{p,H_2O}^g = 1.180\times10^{-6}T^2 + 9.621\times10^{-3}T + 30.326 \tag{2-96}$$

The specific heat capacities of solid and liquid phases change slightly with temperature [34]. Consequently, the specific heat capacities of platinum, carbon black, liquid water and membrane/ionomer are assumed as temperature-independent constants of 1.3×10^2, 894.4, 1090.0 and 4187.0 (J kg^{-1} K^{-1}), respectively. The expressions for the thermal conductivities of hydrogen, oxygen, nitrogen and water vapour are:

$$k_{H_2} = 3.777\times10^{-4}T + 7.444\times10^{-2} \tag{2-97}$$

$$k_{O_2} = 6.204\times10^{-5}T + 8.83\times10^{-3} \tag{2-98}$$

$$k_{N_2} = 5.453\times10^{-5}T + 1.088\times10^{-2} \tag{2-99}$$

$$k_{H_2O}^g = 1.188\times10^{-4}T - 2.404\times10^{-2} \tag{2-100}$$

For the solid components, e.g., platinum, carbon black and liquid water, the expressions for the thermal conductivities are:

$$k_{Pt} = -5.037\times10^{-9}T^3 + 2.483\times10^{-5}T^2 - 2.282\times10^{-2}T + 77.80 \tag{2-101}$$

$$k_C = 1.048\times10^{-6}T^2 - 2.869\times10^{-3}T + 2.979 \tag{2-102}$$

$$k^l_{H_2O} = -1.118\times10^{-5}T^2 + 8.388\times10^{-3}T - 0.9004 \tag{2-103}$$

It is worth noting that Eqs. (2-93) – (2-103) are obtained through the best fit of experimental data [26]. The effective thermal conductivity and specific heat capacity are dependent on the volume fractions of the species within a chosen domain. Without a doubt, the cathode catalyst layer is the most complicated domain in which gas mixture, liquid water, ionomer, Pt/C et al. are all involved. The detailed expressions for the effective thermal conductivity and specific heat capacity of GDL, CL, and membrane/ionomer are listed in Table 2.2.

Table 2.2 Effective specific heat capacity and thermal conductivity of GDL, CL and membrane.

	GDL	*CL*	*Membrane*
c_p^{eff}	$(1-\varepsilon_{GDL})c_{p,C} + s\varepsilon_{GDL}c^l_{p,w} + (1-s)\varepsilon_{GDL}c^g_p$	$L_{Pt}c_{p,Pt} + (L_C + L_S)c_{p,C} + L_M c_{p,M} + s\varepsilon_{CL}c^l_{p,w} + (1-s)\varepsilon_{CL}c^g_p$	$c_{p,M}$
k^{eff}	$(1-\varepsilon_{GDL})k_C + s\varepsilon_{GDL}k^l_w + (1-s)\varepsilon_{GDL}k^g_p$	$L_{Pt}k_{Pt} + (L_C + L_S)k_C + L_M k_M + s\varepsilon_{CL}k^l_w + (1-s)\varepsilon_{CL}k^g_p$	k_M

4. Electrode properties

4.1 Porosity of the catalyst layer

The total volume of CL consists of five components, including ionomer (M), platinum (Pt), carbon black (C), void space (P) and solid intrusion (S), e.g., the penetration of GDL into CL.

$$V_{tot} = V_M + V_{Pt} + V_C + V_P + V_S \tag{2-104}$$

where the volume of the void space consists of two parts: primary pores ($V_{P,p}$) and secondary pores ($V_{P,s}$).

The primary pores are the void space within the agglomerates and the secondary pores are the void space between the agglomerates, thus we have:

$$V_P = V_{P,p} + V_{P,s} \tag{2-105}$$

The Pt/C is constructed by platinum and carbon, thus

$$V_{Pt/C} = V_{Pt} + V_C \tag{2-106}$$

Dividing both sides of Eq. (2-104) by the total volume of the catalyst layer (V_{tot}), the sum of volume fractions of all components is equal to unity, leading to

$$1 = L_M + L_{Pt} + L_C + L_S + \varepsilon_{CL} \tag{2-107}$$

$$\varepsilon_{CL} = \varepsilon_p + \varepsilon_s \tag{2-108}$$

where the terms on the right side of Eq. (2-107) represent the volume fraction of ionomer (L_M), platinum (L_{Pt}), carbon (L_C), solid portion (L_S), primary pores (ε_p), and secondary pores (ε_s), respectively, which are written as:

$$L_M = \frac{V_M}{V_{tot}},\ L_{Pt} = \frac{V_{Pt}}{V_{tot}},\ L_C = \frac{V_C}{V_{tot}},\ L_S = \frac{V_S}{V_{tot}},\ \varepsilon_p = \frac{V_{P,p}}{V_{tot}},\ \varepsilon_s = \frac{V_{P,s}}{V_{tot}} \tag{2-109}$$

The volume fraction of platinum, carbon and ionomer were related to their mass loading and densities and CL thickness (δ_{CL}) as

$$L_{Pt} = \frac{m_{Pt}}{\rho_{Pt}\delta_{CL}},\ L_C = \frac{m_C}{\rho_C\delta_{CL}},\ L_M = \frac{m_M}{\rho_M\delta_{CL}} \tag{2-110}$$

Normally, platinum is dispersed in carbon black to construct the catalyst particles. Therefore, the volume fraction of Pt/C is the sum of the volume fractions of platinum and carbon, which can be written as [2]:

$$L_{Pt/C} = \frac{m_{Pt}}{\delta_{CL}}\left(\frac{1}{\rho_{Pt}} + \frac{1-f}{f}\frac{1}{\rho_C}\right) \tag{2-111}$$

where the platinum mass ratio to that of carbon (abbreviated as platinum mass ratio) is defined as:

$$f = \frac{m_{Pt}}{m_{Pt} + m_C} \tag{2-112}$$

Due to the clamping force of the membrane electrode assembly (MEA), the intrusion of GDL into CL occurs. The volume fraction of the solid portion of the catalyst layer is defined as:

$$L_S = L_{GDL}(1-\varepsilon_{GDL}) \tag{2-113}$$

where L_{GDL} is the percentage of GDL penetrating the catalyst layer and, ε_{GDL} is GDL porosity. The CL porosity is therefore being written as:

$$\varepsilon_{CL} = 1 - L_M - L_{GDL}(1-\varepsilon_{GDL}) - \frac{m_{Pt}}{\delta_{CL}}\left(\frac{1}{\rho_{Pt}} + \frac{1-f}{f}\frac{1}{\rho_C}\right) \tag{2-114}$$

Note that two unknown variables are in the above expression, ε_{CL} and δ_{CL}. There are two approaches to using the above equation. One is to fix the CL thickness and calculate the CL porosity, the other is to fix the CL porosity and calculate the CL thickness. According to the CL preparation process, when the CL is prepared on the GDL or membrane, a hot press is required to reduce the contact resistance between different layers. Therefore, most of the models fixed CL thickness as a constant and study the variation of CL porosity as a function of other parameters, e.g., platinum loading and platinum mass ratio [35, 36]. Other studies showed that the CL thickness increases when the platinum loading increases and the CL porosity is approximately maintained as a constant. Therefore, fixing the CL porosity as a constant is a better approach. Nevertheless, a good agreement can be achieved for the CL thickness as a function of the Pt loading when modeling results are compared with the experimental data (Figure 2.7).

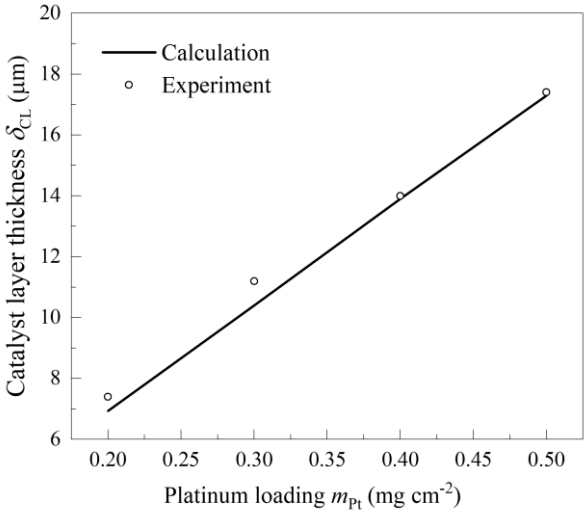

FIGURE 2.7 Catalyst layer thickness with different Pt loadings in base-case condition. Experimental data from Lee et al [37].

4.2 Agglomerate density

Ionomer first partially fills up the primary pores within the agglomerate and then covers the agglomerate to form a thin film. The total volume of ionomer is:

$$V_M = V_{M,agg} + V_{M,\delta} \tag{2-115}$$

where $V_{M,agg}$ (m^3) is the volume of ionomer within the agglomerate and, $V_{M,\delta}$ (m^3) is the volume of ionomer that existed as the thin film surrounding the agglomerate. Since the agglomerate particles consist of Pt/C, ionomer and primary pores, the total volume of the agglomerate is:

$$V_{agg,tot} = V_{Pt/C} + V_{M,agg} + V_{P,p} \tag{2-116}$$

The volume fraction of ionomer within the agglomerate ($\varepsilon_{agg,M}$) and the volume fraction of primary pore space within the agglomerate ($\varepsilon_{agg,p}$) are introduced as:

$$\varepsilon_{agg,M} = \frac{V_{M,agg}}{V_{agg,tot}}, \quad \varepsilon_{agg,p} = \frac{V_{P,p}}{V_{agg,tot}} \tag{2-117}$$

The total volume of the agglomerate could be calculated through the combination of the above two expressions.

$$V_{agg,tot} = \frac{V_{Pt/C}}{1 - \varepsilon_{agg,M} - \varepsilon_{agg,p}} \tag{2-118}$$

The volume of the individual agglomerate particle (without the ionomer film) is

$$V_{agg,i} = \frac{4}{3}\pi r_{agg}^3 \tag{2-119}$$

Dividing Eq. (2-118) by Eq. (2-119), the total number of the agglomerates is found as:

$$n_{agg} = \frac{3V_{Pt/C}}{4(1 - \varepsilon_{agg,M} - \varepsilon_{agg,p})\pi r_{agg}^3} \tag{2-120}$$

Defining the number of agglomerate particles per volume of the catalyst layer, the agglomerate density is introduced as

$$N_{agg} = \frac{3L_{Pt/C}}{4(1 - \varepsilon_{CL})\pi r_{agg}^3} \tag{2-121}$$

4.3 Thicknesses of the ionomer and liquid water films

The volume of agglomerate with the ionomer film is equal to the volume of Pt/C, ionomer and primary pores, leading to:

$$n_{agg}\frac{4}{3}\pi(r_{agg} + \delta_M)^3 = V_M + V_{Pt/C} + V_{P,p} \tag{2-122}$$

Substituting Eq. (2-122) into Eq. (2-104) leads to

$$V_{tot} = n_{agg} \frac{4}{3} \pi (r_{agg} + \delta_M)^3 + V_{P,s} + V_S \tag{2-123}$$

Substituting the total number of agglomerates Eq. (2-120) into the above equation and then dividing both sides by V_{tot} gives

$$1 = \frac{L_{Pt/C}(r_{agg} + \delta_M)^3}{(1-\varepsilon_{CL}) r_{agg}^3} + \varepsilon_s + L_S \tag{2-124}$$

The volume fractions of the primary and secondary pores are:

$$\varepsilon_p = \frac{L_{Pt/C}(\varepsilon_{CL} - \varepsilon_{agg,M})}{1-\varepsilon_{CL}} \tag{2-125}$$

$$\varepsilon_s = \varepsilon_{CL} - \frac{L_{Pt/C}(\varepsilon_{CL} - \varepsilon_{agg,M})}{1-\varepsilon_{CL}} \tag{2-126}$$

By substituting Eq. (2-126) into Eq. (2-124), the thickness of the ionomer thin film can be calculated by the following equation:

$$\delta_M = r_{agg} \left[\sqrt[3]{\frac{(1-\varepsilon_{CL})(1-\varepsilon_{CL}-L_S) + L_{Pt/C}(\varepsilon_{CL} - \varepsilon_{agg,M})}{L_{Pt/C}}} - 1 \right] \tag{2-127}$$

Defining the volume fraction of the primary pores occupied by the ionomer as:

$$\%M = \frac{\varepsilon_{agg,M}}{\varepsilon_{agg,M} + \varepsilon_{agg,p}} \tag{2-128}$$

Then Eq. (2-128) becomes to:

$$\delta_M = r_{agg} \left[\sqrt[3]{\frac{(1-\varepsilon_{CL})(1-\varepsilon_{CL}-L_S) + L_{Pt/C}\varepsilon_{CL}(1-\%M)}{L_{Pt/C}}} - 1 \right] \tag{2-129}$$

If the primary pores are completely occupied by the ionomer ($\%M = 1$), the above expression changes to:

$$\delta_M = r_{agg} \left[\sqrt[3]{\frac{(1-\varepsilon_{CL})(1-\varepsilon_{CL}-L_S)}{L_{Pt/C}}} - 1 \right] \tag{2-130}$$

It is important to note that the volume fraction of the ionomer with the agglomerate ($\varepsilon_{agg,M}$) is impossible to larger than the porosity of the catalyst layer (ε_{CL}).

Assuming that the ionomer is hydrophilic, any liquid water is assumed to coat the entire surface of the individual agglomerate to generate a liquid water film adjacent to the outer boundary of the ionomer film. The total volume of the liquid water generated can be obtained as:

$$V_w = s\varepsilon_{CL} V_{tot} \tag{2-131}$$

where s is the liquid water saturation, which is defined as the volume fraction of the void space occupied by liquid water.

Averaging the total volume of the liquid water to each agglomerate, the volume of the liquid water surrounding each agglomerate is:

$$V_{w,i} = \frac{s\varepsilon_{CL}}{N_{agg}} \tag{2-132}$$

Then the liquid water film thickness is given as:

$$\delta_w = \sqrt[3]{(r_{agg} + \delta_M)^3 + \frac{3s\varepsilon_{CL}}{4\pi N_{agg}}} - (r_{agg} + \delta_M) \tag{2-133}$$

4.4 Specific area

For CLs prepared through spraying catalyst ink onto GDLs, that consists of Pt catalyst dispersed in Vulcan XC72 carbon black, Nafion solution (5%), and organic solvent, e.g., glycerol and isopropanol, the reaction surface area per unit platinum mass (m^2 kg^{-1}) can be roughly calculated by the following empirical expression [32, 38]:

$$A_s = (227.79f^3 - 158.57f^2 - 201.53f + 159.5) \times 10^3 \tag{2-134}$$

where f is the platinum mass fraction. The specific area of the catalyst layer (m^{-1}), defined as the total active area per volume of the catalyst layer, can be written as [2, 15]:

$$a_{CL} = \frac{m_{Pt}}{\delta_{CL}} A_s \tag{2-135}$$

The specific area of the agglomerate, defined as the total active area per volume of agglomerate, could be expressed as [35, 36]:

$$a_{agg} = \frac{m_{Pt} A_s}{\delta_{CL}} \frac{(1 - \varepsilon_{CL})}{L_{Pt/C}} \tag{2-136}$$

4.5 Deformation of porous electrode

To avoid gas leakage and minimize contact resistance, a certain clamping force is applied to the bipolar plates. However, the deformation caused by the clamping force may damage the microstructure of GDL. As the most compressible component in MEA, the deformation of GDL is much more significant than that of the catalyst layer (CL) and PEM [39]. In addition, the deformation of GDL under the rib is more obvious than in the area under the channel owing to the special channel-rib pattern of the flow field [40]. Consequently, non-uniform deformation of GDL results in inhomogeneous variations of the physical properties of GDL under the rib and channel, such as porosity, thickness, permeability, effective diffusivity, and effective

electrical conductivity, which in turn affect the cell performance and durability. These physical properties are competitive and coupled in the transport process in GDL.

Over the past decades, numerous experimental and numerical studies have been reported on GDL deformation and the associated effect on cell performance [41-43]. Imaging techniques such as synchrotron X-ray imaging [44] and X-ray computed tomography [45] have been widely used to investigate the microstructural changes of GDL under clamping force. For example, Zenyuk et al. [46] and Tötzke et al. [47] utilized X-ray computed tomography (CT) to explore the microstructural change, such as porosity, tortuosity, and pore-size distribution (PSD) of different GDL materials under various levels of compression loads, concluding that the porosity decreased with compression and the PSD shifted from bimodal to unimodal while the larger pores were shifted to that of the smaller radii. Atkinson et al. [48] investigated the variation of the porosity and ohmic resistance of different GDL types under varying degrees of compression on the influence of the mass transport resistance via X-ray CT and found that the concentration losses increased with compression owing to the decreased porosity. The morphological properties of the entire MEA with two distinct flow field arrangements under different compression ratios were investigated by Kulkarni et al. [49] and found that the symmetrical flow field arrangement had a smaller deformation compared to the asymmetrical flow field arrangement when the compression ratio was lower than 40%. However, a higher compression would lead to the delamination of MEA in the symmetrical flow field arrangement. The polarization curves of a fuel cell under varying clamping pressure were tested by Chang et al. [50] using a homemade test fixture with three different types of GDLs. Their results indicated the existence of optimal clamping pressure to maximize the peak power density and the optimal value was approximately 3.0 MPa in their experiments. These experimental studies revealed the variation of the morphological properties of the MEA components under realistic compression conditions and qualitatively measured the effect of the clamping pressure on the physical properties of GDLs, such as porosity, permeability, gas diffusivity and electrical/thermal conductivity. All these experimental studies provided a comprehensive dataset for computational modelling.

With respect to the numerical studies of the influence of the GDL deformation on the transport properties and cell performance, not only the variation of physical properties of GDL, but also the effect of the compression on the current density distribution and liquid water distribution in an operating fuel cell, which are infeasible or costly to be measured by experimental approaches. For example, Li et al. [42] developed a three-dimensional, two-phase PEMFC model to investigate the local current density distribution at various assembly pressure. They found that the local current density under the channel is higher than that under the rib and the non-uniform was more serious with increasing compression. Jiao et al. [51] investigated the

effect of compression on the water transport in GDLs using OpenFOAM, concluding that the compression increased the flow resistance for the liquid water and the vapor, which led to an uneven distribution of fluids. Mehrtash et al. [52] developed a two-dimensional, half-cell, non-isothermal, multi-phase model to study the variation of the water concentration and current density profiles, as well as characterization curves, with respect to different levels of compression. Zhou et al. [53] used the finite element method (FEM) to analyse the relationship between GDL deformation and cell performance. The numerical results showed that the increase in compressive deformation deteriorated the cell performance when the contact resistance was not considered and there existed an optimal clamping pressure when the contact resistance was considered.

The clamping force required to achieve different levels of electrode deformation is calculated as follows:

$$\frac{\partial \sigma_{ij}}{\partial x_j} + b_i = 0 \tag{2-137}$$

$$\frac{\partial^2 \varepsilon_{ij}}{\partial x_k \partial x_l} + \frac{\partial^2 \varepsilon_{kl}}{\partial x_i \partial x_j} - \frac{\partial^2 \varepsilon_{ik}}{\partial x_j \partial x_l} - \frac{\partial^2 \varepsilon_{jl}}{\partial x_i \partial x_k} = 0 \tag{2-138}$$

where σ_{ij} (Pa) is the stress tensor, b_i is the body force vector, and ε_{ij} is the strain tensor. Eq. (2-137) indicates that the displacement within the electrodes is single-valued and continuous. Typically, only the deformation of the GDLs is considered because the deformation of the other components, including the membrane and CLs, is very limited owing to either the higher mechanical strength or the smaller dimensions.

Based on Hooke's law for linear elastic deformation, the stress and strain are related through the following constitutive relation:

$$\sigma_{ij} = \lambda \delta_{ij} \varepsilon_{kk} + 2\mu \varepsilon_{ij} \tag{2-139}$$

$$\lambda = \frac{E\nu}{(1+\nu)(1-2\nu)},\ \mu = \frac{E}{2(1+\nu)} \tag{2-140}$$

where E (Pa) is Young's modulus, ν is the Poisson ratio, δ_{ij} is the Kronecker delta, and the subscripts *i*, *j*, and *k* are the coordinates of the computational domain. The required stress to achieve the desired compression ratio of the GDLs could be calculated.

The GDL porosity after compression and the compression ratio (*CR*) can be calculated as [54]

$$\varepsilon_{GDL} = \frac{\varepsilon_{GDL}^0 - CR}{1 - CR} \tag{2-141}$$

$$CR = 1 - \delta' / \delta^0 \tag{2-142}$$

where *CR* is defined as the ratio of the GDL thickness before and after compression, δ^0 and δ' are the thicknesses of the initial and compressed GDL, respectively. ε_{GDL}^0 represents the initial GDL porosity and the ε_{GDL} is the GDL porosity after compression.

5. Water management

Water exists in three phases: vapour, liquid water and the dissolved phase in membrane and ionomer. Due to the hydrophilic property of the Nafion ionomer, water uptake occurs when the membrane and ionomer are exposed to a humidified environment.

5.1 Water phase-transfer and water transport through membrane

Water exists in three different phases in different solvents [55-57], including the dissolved water in the membrane and ionomer, water vapour and liquid water in the porous media and flow channels. The dissolved water is the membrane and ionomer absorbed water, which enters the membrane and ionomer from the water vapour during water uptake and leaves the membrane and ionomer in the liquid phase when the water content of the membrane and ionomer exceeds complete saturation. The main phase transfer mechanisms include the following processes: the phase transfer between liquid water and water vapour via condensation and evaporation, the phase transfer between dissolved water and water vapour through membrane and ionomer absorption or water uptake, and the phase transfer between liquid water and dissolved water during membrane and ionomer desorption.

Water transport in the membrane plays an important role in determining the water content in the membrane/ionomer [28, 55-58]. During fuel cell operation, water transport through the membrane occurs via three mechanisms: electro-osmotic drag (EOD) of water molecules carried by protons migrating from anode to cathode, back diffusion driven by the concentration gradient of water, and convection generated by the pressure gradient. We can mathematically describe the dissolved water transport through the membrane as:

$$\frac{\partial}{\partial t}(L_M c_w^d) + \nabla \cdot (n_d \frac{i_M}{F}) - \nabla \cdot (D_{w-M} \nabla c_w^d) - \nabla \cdot \left(\frac{k_{p,M} c_w^d}{\mu_w} \nabla p \right) = S_w^d \tag{2-143}$$

The term on the left-hand side refers to the water accumulation, water migration by electro-osmotic drag, back diffusion and hydraulic permeation, respectively. L_M is the volume fraction of ionomer (L_M = 1 in the membrane, 0 < L_M <1 in the catalyst layer, L_M = 0 in GDL and channel), c_w^d (mol m^{-3}) is the concentration of the dissolved water, n_d is the EOD

coefficient, which is expressed as $2.5\lambda/22$ [55-59], D_{w-M} (m^2 s) is the diffusion coefficient of water through the membrane, $k_{p,M}$ (m^2) is the hydraulic permeability of water in the membrane, μ_w (Pa s) is the water viscosity, p (Pa) is the pressure, and S_w^d (mol m^{-3} s^{-1}) is the source term of dissolved water. The concentration of the dissolved water depends on the water content of the membrane and ionomer according to the following expression [58]:

$$c_w^d = \frac{\rho_M}{EW}\frac{\lambda}{1+k_s\lambda} \tag{2-144}$$

where ρ_M (kg m^{-3}) is the density of dry membrane, EW (g mol^{-1}) is the equivalent weight of membrane and k_s is the swelling coefficient, representing the volume increase of the membrane and ionomer.

The polymeric matrix of the membrane and ionomer expands leading to an increase in their volume when membrane/ionomer water absorption (water uptake) occurs. Normally a dry Nafion® membrane/ionomer swells approximately 20% when fully hydrated by water vapour [58, 60]. Membrane and ionomer swelling has two effects on fuel cell performance. For the membrane, higher swelling increases the ionic conductivity and water diffusion coefficient, while for the ionomer, higher swelling increases the thickness of the ionomer film surrounding the agglomerate and decreases the void space within the catalyst layer, leading to an increase in transport resistance of reactant gases, especially the oxygen [58].

Depending on the directions of membrane swelling, there are two types of membrane deformation: the through-plane membrane thickness increasing and the in-plane membrane buckling. The through-plane membrane thickness increase is caused by the zero or low fastening force from gas flow fields to the MEA [61]. Since the membrane is fixed between the bipolar plates under a relatively high clamping force, the thickness of the portion of the membrane under the current collector ribs is impossible to change during membrane water absorption (water uptake). However, the in-plane buckling occurs under the channels as shown in Figure 2.8. Compared to the through-plane thickness increasing, the in-plane buckling is more important as the in-plane stress is the major stress component in the membrane [62]. The in-plane buckling could have a significant impact on the channel flow as the MEA bulges into the channel. The bulged GDL into the flow channels increases the mass transport resistance and can lead to pinhole formation of the membrane under the channel [63]. The volume fraction of the ionomer within CL after swelling is calculated by the following equation:

$$L_M^{swell} = L_M(1+k_s\lambda) \tag{2-145}$$

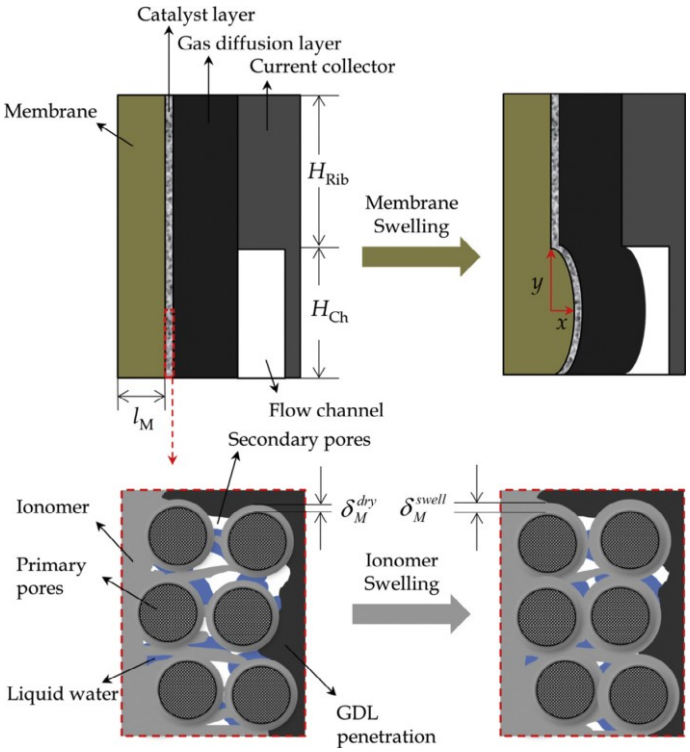

FIGURE 2.8 Sketch of the membrane and ionomer swelling and the bulged MEA into the flow channel. *Credit: Reprinted from Xing et al., Applied Energy, **138**, 242–257, 2015, with permission from Elsevier.*

Dissolved water is absorbed by the membrane and ionomer when the concentration of the dissolved water is smaller than the equilibrium concentration, which is the maximum dissolved water being carried by the membrane and ionomer. After reaching the equilibrium concentration, the dissolved water moves away from the membrane and ionomer in the liquid water phase, during the process of membrane and ionomer desorption. The source terms regarding the process above are:

$$S_w^{vd} = k_{ads}(c_w^{eq} - c_w^d) \qquad c_w^d < c_w^{eq} \tag{2-146}$$

$$S_w^{dl} = k_{des}(c_w^d - c_w^{eq}) \qquad c_w^d \geq c_w^{eq} \tag{2-147}$$

The subscripts *vd* and *dl* in the source term represent the water phase change from vapour to dissolved water and from dissolved water to liquid water, respectively. k_{ads} and k_{des} (s^{-1}) are the adsorption and desorption rate coefficient, given by [59, 64]:

$$k_{ads} = \frac{1.14\times10^{-5} f_w}{\delta_{CL}} \exp\left[2416\left(\frac{1}{303} - \frac{1}{T}\right)\right] \tag{2-148}$$

$$k_{des} = \frac{4.59\times10^{-5} f_w}{\delta_{CL}} \exp\left[2416\left(\frac{1}{303} - \frac{1}{T}\right)\right] \tag{2-149}$$

$$f_w = \frac{\lambda V_w}{V_M + \lambda V_w} \tag{2-150}$$

Where f_w is the water volume fraction of the membrane, V_w and V_M (m^3 mol^{-1}) are the partial molar volume of water and the dry membrane, respectively. c_w^{eq} (mol m^{-3}) is the equilibrium dissolved water concentration, which is determined by the equilibrium water content according to Eq. (2-144). The equilibrium water content is given by empirical correlations based on water uptake measurements [57], given as:

$$\lambda^{eq} = 16.8s + 14.0(1-s) \qquad s > 0 \tag{2-151}$$

where s is the liquid water saturation. The actual water content as a function of water activity is

$$\lambda = 0.043 + 17.81\alpha_{H_2O} - 39.85\alpha_{H_2O}^2 + 36.0\alpha_{H_2O}^3 \qquad \alpha_{H_2O} \le 1 \tag{2-152}$$

In the above equation, α_{H_2O} can be a function of both water vapour partial pressure and liquid water saturation [56], as given below:

$$\alpha_{H_2O} = x_w \frac{p}{p_{sat}} + 2s \tag{2-153}$$

5.2 Diffusion of species in Nafion ionomer with different membrane water content

According to the agglomerate assumption, reactant gases must diffuse through the ionomer film surrounding the agglomerate before reaching the surface of platinum catalyst particles inside the agglomerate. Owing to the much higher solubility and diffusivity of hydrogen through Nafion® than that of oxygen, the diffusion of oxygen through the ionomer film is more critical [4, 15]. For oxygen diffusivity through the Nafion® membrane and ionomer, Marr and Li [15] provided a temperature-dependent equation by fitting the experimental data published by Parthasarathy et al. [18]. Suzuki et al. [65] reported that the oxygen diffusion coefficient is proportional to the power of the membrane water content. Using the combination of the two expressions and the influence of temperature and membrane water content, and the following expression can be obtained.

$$D_{O_2-M} = 1.3926\times10^{-10}\lambda^{0.708}\exp\left(\frac{T-273}{106.65}\right) - 1.6461\times10^{-10}\lambda^{0.708} + 5.2\times10^{-10} \tag{2-154}$$

where λ and T (K) are membrane/ionomer water content and temperature, respectively.

Conversely, Henry's constant for oxygen solubility in the Nafion® ionomer depends on the relative humidity [66]. To investigate the effect of water content on Henry's constant, one can

calculate Henry's constant from the expression given below, which is obtained by modifying the equation of Marr and Li [15] and fitting the results of Suzuki et al. [65]:

$$H_{O_2} = 0.11552 \exp\left(14.1 + 0.0302\lambda - \frac{666}{T}\right) \tag{2-155}$$

A comparison of Eq. (2-154) with the experimental data of Takamura et al. [67] and Eq. (2-155) with the simulation results of Suzuki et al. [65] is shown in Figure 2.9.

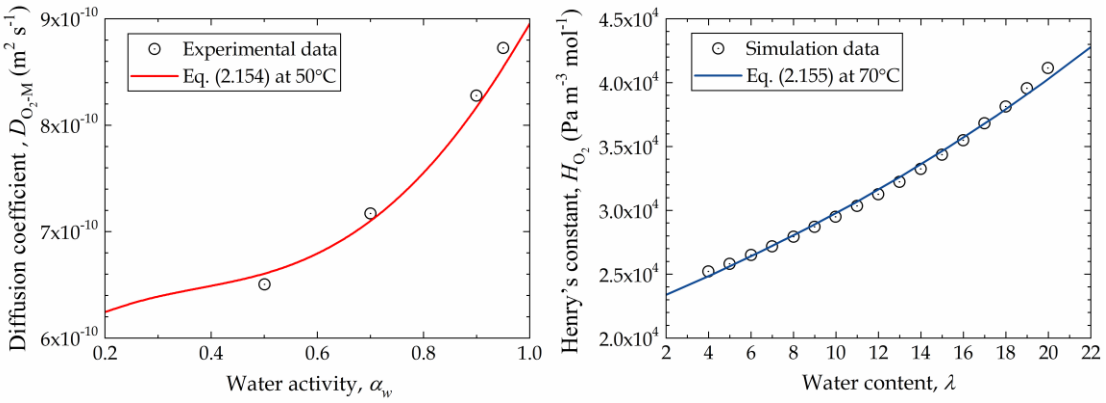

FIGURE 2.9 Oxygen diffusivity through Nafion® membrane/ ionomer as a function of water activity (left) and Henry's constant for oxygen solubility in Nafion® membrane/ ionomer as a function of water content (right).

Nafion® is an ideal media for dissolved water transport, the diffusion coefficient of water through the membrane is a piecewise function that can be determined by both temperature and membrane water content [4, 10, 28, 32, 38, 55-58, 60, 68]:

$$D_{H_2O-M} = \begin{cases} D_0(2.563 - 0.33\lambda + 0.0264\lambda^2 - 0.000671\lambda^3) & \lambda > 4 \\ D_0(-1.25\lambda + 6.65) & 3 < \lambda \le 4 \\ D_0(2.05\lambda - 3.25) & 2 \le \lambda \le 3 \end{cases} \tag{2-156}$$

$$D_0 = 1.0 \times 10^{-10} \exp\left[2416\left(\frac{1}{303} - \frac{1}{T}\right)\right] \tag{2-157}$$

For the above expressions, the membrane water content (λ) can be calculated from the water activity (α_w) using the following expression:

$$\lambda = \begin{cases} 0.043 + 17.81\alpha_w - 39.85\alpha_w^{\ 2} + 36.0\alpha_w^{\ 3} & \alpha_w < 1 \\ 14.0 + 1.4(\alpha_w - 1) & 1 \le \alpha_w \le 3 \\ 16.8 & \alpha_w > 3 \end{cases} \tag{2-158}$$

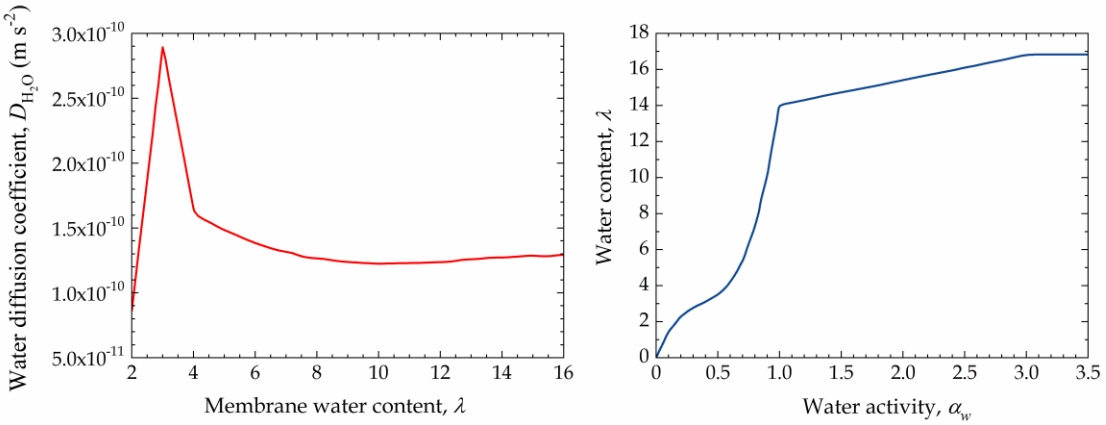

FIGURE 2.10 Water diffusion coefficient through the membrane (left) and the relationship between water activity and membrane water content (right) of Nafion® 117 at 30°C.

Figure 2.10 shows the water diffusion coefficient through Nafion® membrane as a function of membrane water content and the relationship between water activity with membrane water content. As shown in Figure 2.10, when the membrane water content increases, the diffusion coefficient initially increases and then decreases to a constant, while the membrane water content increases up to 16.8 as water activity increases. Water activity can be associated with the partial pressure of water vapour as [69]:

$$\alpha_w = \frac{p_w}{p_{sat}} = RH \tag{2-159}$$

where p_w (Pa) is the partial pressure of water vapour, p_{sat} (Pa) is the saturated water vapour pressure, which is the water vapour pressure at saturation temperature, and *RH* is the relative humidity. The saturated water pressure is obtained by fitting the experimental data. A polynomial equation is given as

$$\begin{aligned} p_{sat} = {} & 9.531\times10^{-4}(T-237)^4 - 3.123\times10^{-2}(T-237)^3 \\ & + 3.451(T-237)^2 + 20.96(T-237) + 611.0 \end{aligned} \tag{2-160}$$

Water could also diffuse through the Nafion® membrane under a pressure force, the hydraulic permeability of water through Nafion® is associated with the membrane water content as [4]:

$$k_{p,M} = 2.86\times10^{-20}\lambda \tag{2-161}$$

5.3 Two-phase flow of gas-water mixture

The generation of water is unavoidable during the operation of PEMFCs owing to the oxygen reduction reaction and water migration under electro-osmotic drag. Water is typically formed at the cathode side. However, the consumption of hydrogen at the anode side could also trigger the formation of liquid water at high relative humidity because the vapour is oversaturated. At

a steady-state condition, applying the continuity equation on liquid water and gas phase, respectively, the following equations are obtained:

$$\nabla \cdot (\rho_w^l \mathbf{u}_w^l) = M_w S_l \tag{2-162}$$

$$\nabla \cdot (\rho_w^g \mathbf{u}_w^g) = M_w S_g \tag{2-163}$$

where M_w (kg mol^{-1}) is the molecular weight of water and, ρ (kg m^{-3}), $\mathbf{u}$ (m s^{-1}) and S (mol m^{-3} s^{-1}) are the density, velocity and source term of liquid water and water vapour, respectively. The subscript *w* represents water, and the superscripts *l* and *g* represent the liquid water and gas phase, respectively.

According to Darcy's law, the velocity of the liquid water and gas phase can be related to their partial pressure as:

$$\mathbf{u}_w^l = -\frac{K^l}{\mu_w^l} \nabla p^l \tag{2-164}$$

$$\mathbf{u}_w^g = -\frac{K^g}{\mu_w^g} \nabla p^g \tag{2-165}$$

where K (m^2), μ (Pa s) and p (Pa) are the permeability, viscosity and partial pressure of the liquid water and gas phase, respectively. The pressure difference between the wetting and non-wetting phase within the porous media is the capillary pressure (p^c), which is expressed as:

$$p^c = p^g - p^l \tag{2-166}$$

Substituting Eq. (2-166) into Eq. (2-164), the liquid water velocity becomes to:

$$\mathbf{u}_w^l = \frac{K^l}{\mu_w^l} \nabla p^c - \frac{K^l}{\mu_w^l} \nabla p^g \tag{2-167}$$

Introducing the liquid water saturation (*s*), defined as the volume fraction of the liquid water in the porous media, into Eq. (2-167) gives

$$\mathbf{u}_w^l = \frac{K^l}{\mu_w^l} \frac{dp^c}{ds} \nabla s - \frac{K^l}{\mu_w^l} \nabla p^g \tag{2-168}$$

Capillary pressure can be linked to liquid water saturation as [70-73]:

$$p^c = \sigma \cos(\theta_c) \left(\frac{\varepsilon}{K} \right)^{1/2} J(s) \tag{2-169}$$

where $J(s)$ is the Leverett function, and is given by [70-73]:

$$J(s)=\begin{cases}1.417(1-s)-2.120(1-s)^2+1.263(1-s)^3 & \theta_c<90^\circ \\ 1.417s-2.120s^2+1.263s^3 & \theta_c>90^\circ\end{cases} \quad (2\text{-}170)$$

Normally, the porous electrode is hydrophobic, therefore the Leverett function is expressed in terms of the liquid water saturation and the contact angle, θ_c, is between 90° and 180°. The surface tension (σ) for the liquid water-air system is 0.0625 N/m. It is also worth noting that the Leverett *J*-function was originally obtained from the empirical measurement of water transport in unconsolidated sand [70], which may not be appropriate for some diffusion media, e.g., SGL 24 series carbon paper tailored with PTFE content varying from 5 to 20 wt%, due to the inaccurate prediction of capillary pressure at high non-wetting phase saturation [74, 75] and GDLs modified with hydrophobic fluorinated-ethylene-propylene (FEP) or polydimethylsiloxane (PDMS) [76]. The significant hysteresis of capillary pressure of fresh and aged diffusion media was also observed during experiments as reported in Ref. [75].

Combing Eq. (2-168) and Eq. (2-169), the liquid water velocity is expressed in terms of liquid water saturation as:

$$\mathbf{u}_w^l=\sigma\cos(\theta_c)\frac{K^l}{\mu_w^l}\left(\frac{\varepsilon}{K}\right)^{1/2}\frac{dJ(s)}{ds}\nabla s-\frac{K^l}{\mu_w^l}\nabla p^g \quad (2\text{-}171)$$

The permeability of liquid water and gas phase can be associated with the permeability of the porous media via:

$$K^l=k_r^lK\ ,\ \ K^g=k_r^gK \quad (2\text{-}172)$$

where k_{rl} and k_{rg} are the relative permeability of liquid water and gas phase, which are proportional to the cube of liquid water saturation as:

$$k_r^l=s^3\ ,\ \ k_r^g=(1-s)^3 \quad (2\text{-}173)$$

Substituting Eq. (2-165) and Eq. (2-172) into Eq. (2-171) leads to:

$$\mathbf{u}_w^l=\frac{\sigma\cos(\theta_c)k_r^l}{\mu_w^l}(\varepsilon K)^{1/2}\frac{dJ(s)}{ds}\nabla s-\frac{k_r^l\mu_w^g}{k_r^g\mu_w^l}\mathbf{u}_w^g \quad (2\text{-}174)$$

Substituting Eq. (2-174) into Eq. (2-162) and taking the liquid water accumulation into account, the liquid water saturation can be calculated as:

$$\frac{\partial}{\partial t}(\varepsilon\rho_w^ls)+\nabla\cdot\left(\rho_w^lD_c\nabla s-\frac{\rho_w^lk_r^l\mu_w^g}{k_r^g\mu_w^l}\mathbf{u}^g\right)=M_wS_w^l \quad (2\text{-}175)$$

where D_c ($m^2\ s^{-1}$) is the capillary diffusion coefficient, which is represented by the following expression:

$$D_c = \frac{\sigma \cos(\theta_c) k_r^l}{\mu_w^l} (\varepsilon K)^{1/2} \frac{dJ(s)}{ds} \tag{2-176}$$

At a steady state, if the velocity of the gas phase can be neglected, Eq. (2-175) becomes a second-order partial differential equation for the liquid water saturation:

$$\nabla^2 s = \frac{M_w}{\rho_w^l D_c} S_w^l \tag{2-177}$$

The right-hand term of the above equation is the source term, which includes the water production from the reaction and water phase change. The conservation of water in different domains of PEMFCs are given in Table 2.3, in which the superscripts *v*, *l*, *d* represent water in vapour, liquid and dissolved phases, and superscript *r* represents water generation through reaction.

Table 2.3 Conservation of water in different domains of PEMFCs

	Channel	*GDL*	*CL*
Water vapour, S_w^v	$-S_w^{vl}$	$-S_w^{vl}$	$-S_w^{vd}-S_w^{vl}$
Liquid water, S_w^l	S_w^{vl}	S_w^{vl}	$S_w^{dl}+S_w^{vl}$
Dissolved water, S_w^d	0	0	$S_w^r+S_w^{vd}-S_w^{dl}$

The expressions of water phase change due to membrane and ionomer water uptake and desorption, S_w^{vd} and S_w^{dl}, could be found in Eqs. (2-146) and (2-147). Since the generated water in CL is assumed in the dissolved phase, the source term of water generation through reaction, S_w^r (mol $m^{-3}\ s^{-1}$), is expressed as $-i_c/2F$. The source term, S_w^{vl} (mol $m^{-3}\ s^{-1}$), is introduced for the interfacial mass transfer rate of water by condensation and evaporation, which is defined as:

$$S_w^{vl} = \begin{cases} k_{con} \dfrac{\varepsilon(1-s)x_w^g}{RT}(x_w^g p^g - p_{sat}) & x_w^g p^g \geq p_{sat} \\ k_{eva} \dfrac{\varepsilon s \rho_w^l}{M_w}(p_{sat} - x_w^g p^g) & x_w^g p^g < p_{sat} \end{cases} \tag{2-178}$$

where k_{con} (s^{-1}) and k_{eva} ($atm^{-1}\ s^{-1}$) are the condensation and evaporation rate coefficient, respectively, and x_w^g is the mole fraction of water vapour.

6. Summary

In this chapter, the fundamentals and principles of a typical PEMFC operated with hydrogen and air are represented and the governing equations are derived. All the important chemical and physical processes involved in the operation of PEMFCs are described by proper differential and algebraic equations.

This chapter starts with a description of electrochemical kinetics through both the Butler-Volmer equation and the agglomerate model. Followed by the momentum transport and multi-component mass through the channel and porous electrodes, and heat transport within entire the fuel cell unit. A series of equations are then developed to represent the properties of the catalyst layer, in which the porosity, agglomerate density, thicknesses of ionomer film and liquid water film, and the specific area can be quantitatively obtained. The deformation of the porous electrode is also briefly discussed. As a very important process during PEMFC operation, the water phase transfer and gas-liquid two-phase flow are described by partial differential equations and the source terms responsible for the phase change are given in detail. In addition, the swelling of membrane and ionomer, transport of proton through the membrane, and diffusion of species through the ionomer film are associated with their water content, indicating the importance of membrane hydration during PEMFC operation.

The governing equations build the framework of multi-physics, non-isothermal, and two-phase flow PEMFC models, although the values or expressions of some parameters may change with the development of novel materials and more accurate characterization techniques.

Review Questions

Q1: Calculate the equilibrium potential of the cathode for a fuel cell operating at 80°C and a pressure of 1 atm.

Q2: Calculate the reference exchange current density of the PEMFC cathode for the cell operating at 20, 40, 60, and 80°C.

Q3: Find the effective electronic conductivity for the catalyst layer when the ionomer content is 20% and the porosity of the catalyst layer is 0.3.

Q4: How the ionic conductivity of the ionomer membrane depends on temperature and water content in the membrane? Explain.

References

1. Weber, A.Z., S. Balasubramanian, and P.K. Das, *Chapter 2 - Proton Exchange Membrane Fuel Cells*, in *Advances in Chemical Engineering*, K. Sundmacher, Editor. 2012, Academic Press. p. 65-144.
2. Das, P.K., X. Li, and Z.S. Liu, *Analytical approach to polymer electrolyte membrane fuel cell performance and optimization.* Journal of Electroanalytical Chemistry, 2007. **604**(2): p. 72-90.
3. Weber, A.Z., et al., *A critical review of modeling transport phenomena in polymer-electrolyte fuel cells.* Journal of the Electrochemical Society, 2014. **161**(12): p. F1254-F1299.
4. Bernardi, D.M. and M.W. Verbrugge, *A Mathematical Model of the Solid‐Polymer‐Electrolyte Fuel Cell.* Journal of The Electrochemical Society, 1992. **139**(9): p. 2477-2491.
5. Xing, L., et al., *Inhomogeneous distribution of platinum and ionomer in the porous cathode to maximize the performance of a PEM fuel cell.* AIChE Journal, 2017. **63**(11): p. 4895-4910.
6. Sun, W., B.A. Peppley, and K. Karan, *An improved two-dimensional agglomerate cathode model to study the influence of catalyst layer structural parameters.* Electrochimica Acta, 2005. **50**(16-17): p. 3359-3374.
7. Cheddie, D.F. and N.D.H. Munroe, *Three dimensional modeling of high temperature PEM fuel cells.* Journal of Power Sources, 2006. **160**(1): p. 215-223.
8. Barbir, F., et al., *PEM Fuel Cells : Theory and Practice.* Elsevier Academic Press, 2005.
9. Ismail, M.S., et al., *Effects of anisotropic permeability and electrical conductivity of gas diffusion layers on the performance of proton exchange membrane fuel cells.* Applied Energy, 2012. **95**: p. 50-63.
10. Xing, L., et al., *Multi-variable optimisation of PEMFC cathodes based on surrogate modelling.* International Journal of Hydrogen Energy, 2013. **38**(33): p. 14295-14313.
11. Scharifker and R. B., *The Kinetics of Oxygen Reduction in Molten Phosphoric Acid at High Temperatures.* Journal of The Electrochemical Society, 1987. **134**(11): p. 2714.
12. Vogel, W., et al., *Reaction pathways and poisons—II: The rate controlling step for electrochemical oxidation of hydrogen on Pt in acid and poisoning of the reaction by CO.* Electrochimica Acta, 1975. **20**(1): p. 79-93.
13. Liu, Z., et al., *Study of the oxygen reduction reaction (ORR) at Pt interfaced with phosphoric acid doped polybenzimidazole at elevated temperature and low relative humidity.* Electrochimica Acta, 2006. **51**(19): p. 3914-3923.
14. Birgersson, E., M. Noponen, and M. Vynnycky, *Analysis of a Two-Phase Non-Isothermal Model for a PEFC.* Journal of The Electrochemical Society, 2005. **152**(5): p. A1021.
15. Marr, C. and X. Li, *Composition and performance modelling of catalyst layer in a proton exchange membrane fuel cell.* Journal of Power Sources, 1999. **77**(1): p. 17-27.
16. Liu, Z., Z. Mao, and C. Wang, *A two dimensional partial flooding model for PEMFC.* Journal of Power Sources, 2006. **158**(2): p. 1229-1239.
17. Sousa, T., M. Mamlouk, and K. Scott, *An isothermal model of a laboratory intermediate temperature fuel cell using PBI doped phosphoric acid membranes.* Chemical Engineering Science, 2010. **65**(8): p. 2513-2530.
18. Parthasarathy and Arvind, *Temperature Dependence of the Electrode Kinetics of Oxygen Reduction at the Platinum/Nafion Interface—A Microelectrode Investigation.* Journal of the Electrochemical Society, 1992. **139**(9): p. 2520-2537.

19. Das, P.K., X. Li, and Z.S. Liu, *Effective transport coefficients in PEM fuel cell catalyst and gas diffusion layers: Beyond Bruggeman approximation.* Applied Energy, 2010. **87**(9): p. 2785-2796.
20. Zhou, T. and H. Liu, *Effects of the electrical resistances of the GDL in a PEM fuel cell.* Journal of Power Sources, 2006. **161**(1): p. 444-453.
21. Pantea, D., et al., *Electrical conductivity of conductive carbon blacks: influence of surface chemistry and topology.* Applied Surface Science, 2003. **217**(1-4): p. 181-193.
22. Powell, R.W. and R.P. Tye, *The promise of platinum as a high temperature thermal conductivity reference material.* British Journal of Applied Physics, 1963. **14**(10): p. 662-666.
23. Kamarajugadda, S. and S. Mazumder, *Numerical investigation of the effect of cathode catalyst layer structure and composition on polymer electrolyte membrane fuel cell performance.* Journal of Power Sources, 2008. **183**(2): p. 629-642.
24. Jaouen, F.d.r., G.r. Lindbergh, and G.r. Sundholm, *Investigation of Mass-Transport Limitations in the Solid Polymer Fuel Cell Cathode.* Journal of The Electrochemical Society, 2002. **149**(4): p. A437-A447.
25. Jaouen, F.d.r., G.r. Lindbergh, and K. Wiezell, *Transient Techniques for Investigating Mass-Transport Limitations in Gas Diffusion Electrodes.* Journal of The Electrochemical Society, 2003. **150**(12): p. A1711-A1717.
26. Bird, R., W. Stewart, and E. Lightfoot, *Transport Phenomena*. 2002.
27. Brinkman, H.C., *A calculation of the viscous force exerted by a flowing fluid on a dense swarm of particles.* Applied Scientific Research, 1949. **1**(1): p. 27-34.
28. Springer, T.E., T. Zawodzinski, and S. Gottesfeld, *Polymer Electrolyte Fuel Cell Model.* Journal of The Electrochemical Society, 1991. **138**: p. 2334-2342.
29. Broka, K. and P. Ekdunge, *Modelling the PEM fuel cell cathode.* Journal of Applied Electrochemistry, 1997. **27**(3): p. 281-289.
30. Suzuki, A., et al., *Ionomer content in the catalyst layer of polymer electrolyte membrane fuel cell (PEMFC): Effects on diffusion and performance.* International Journal of Hydrogen Energy, 2011. **36**(3): p. 2221-2229.
31. Xing, L., *Modelling and simulation of the laboratory low temperature proton exchange and direct methanol fuel cells*. 2014, Newcastle University: Newcastle.
32. Khajeh-Hosseini-Dalasm, N., et al., *A study of the agglomerate catalyst layer for the cathode side of a proton exchange membrane fuel cell: Modeling and optimization.* Electrochimica Acta, 2012. **60**: p. 55-65.
33. Wilke, C.R., *A Viscosity Equation for Gas Mixtures.* The Journal of Chemical Physics, 1950. **18**(4): p. 517-519.
34. Poling, B., J. Prausnitz, and J. O'Connell, *The Properties of Gases and Liquids*. 2000.
35. Xing, L., et al., *A two-phase flow and non-isothermal agglomerate model for a proton exchange membrane (PEM) fuel cell.* Energy, 2014. **73**: p. 618-634.
36. Xing, L., et al., *Numerical investigation of the optimal Nafion® ionomer content in cathode catalyst layer: An agglomerate two-phase flow modelling.* International Journal of Hydrogen Energy, 2014. **39**(17): p. 9087-9104.
37. Lee, S.-Y., et al., *Gradient Catalyst Coating for a Proton Exchange Membrane Fuel Cell Operation under Nonhumidified Conditions.* Electrochemical and Solid State Letters, 2007. **10**.
38. Khajeh-Hosseini-Dalasm, N., et al., *A parametric study of cathode catalyst layer structural parameters on the performance of a PEM fuel cell.* International Journal of Hydrogen Energy, 2010. **35**(6): p. 2417-2427.
39. Wu, C.W., et al., *A systematic review for structure optimization and clamping load design of large proton exchange membrane fuel cell stack.* Journal of Power Sources, 2020. **476**: p. 228724.
40. Hottinen, T., et al., *Inhomogeneous compression of PEMFC gas diffusion layer.* Journal of Power Sources, 2007. **171**(1): p. 113-121.

41. Khetabi, E.M., et al., *Effects of mechanical compression on the performance of polymer electrolyte fuel cells and analysis through in-situ characterisation techniques - A review.* Journal of Power Sources, 2019. **424**: p. 8-26.
42. Li, W.Z., et al., *Three-dimensional modeling of a PEMFC with serpentine flow field incorporating the impacts of electrode inhomogeneous compression deformation.* International Journal of Hydrogen Energy, 2019. **44**(39): p. 22194-22209.
43. Holzer, L., et al., *Microstructure-property relationships in a gas diffusion layer (GDL) for Polymer Electrolyte Fuel Cells, Part I: effect of compression and anisotropy of dry GDL.* Electrochimica Acta, 2017. **227**: p. 419-434.
44. Ince, U.U., et al., *Effects of compression on water distribution in gas diffusion layer materials of PEMFC in a point injection device by means of synchrotron X-ray imaging.* International Journal of Hydrogen Energy, 2018. **43**(1): p. 391-406.
45. Bosomoiu, M., G. Tsotridis, and T. Bednarek, *Study of effective transport properties of fresh and aged gas diffusion layers.* Journal of Power Sources, 2015. **285**: p. 568-579.
46. Zenyuk, I.V., et al., *Gas-diffusion-layer structural properties under compression via X-ray tomography.* Journal of Power Sources, 2016. **328**: p. 364-376.
47. Tötzke, C., et al., *A dedicated compression device for high resolution X-ray tomography of compressed gas diffusion layers.* Review of Scientific Instruments, 2015. **86**(4): p. 043702.
48. Atkinson, R.W., et al., *The Role of Compressive Stress on Gas Diffusion Media Morphology and Fuel Cell Performance.* ACS Applied Energy Materials, 2018. **1**(1): p. 191-201.
49. Kulkarni, N., et al., *The effect of non-uniform compression and flow-field arrangements on membrane electrode assemblies - X-ray computed tomography characterisation and effective parameter determination.* Journal of Power Sources, 2019. **426**: p. 97-110.
50. Chang, H. and M. Chang, *Effects of Assembly Pressure on the Gas Diffusion Layer and Performance of a PEM Fuel Cell.* Applied Mechanics and Materials, 2011. **110-116**.
51. Jiao, D., K. Jiao, and Q. Du, *Numerical investigations of vapor condensation and water transport in gas diffusion layers of PEMFC.* International Journal of Heat and Mass Transfer, 2021. **177**: p. 121543.
52. Mehrtash, M., I. Tari, and S. Yesilyurt, *Impacts of inhomogeneous clamping force on local performance and liquid water formation in polymer electrolyte fuel cells.* International Journal of Hydrogen Energy, 2017. **42**(30): p. 19227-19245.
53. Zhou, P. and C.W. Wu, *Numerical study on the compression effect of gas diffusion layer on PEMFC performance.* Journal of Power Sources, 2007. **170**(1): p. 93-100.
54. Wang, Q., et al., *The numerical study of vanadium redox flow battery performance with different electrode morphologies and electrolyte inflow patterns.* Journal of Energy Storage, 2021. **33**: p. 101941.
55. Wu, H., P. Berg, and X. Li, *Steady and unsteady 3D non-isothermal modeling of PEM fuel cells with the effect of non-equilibrium phase transfer.* Applied Energy, 2010. **87**(9): p. 2778-2784.
56. Yang, X.-G., Q. Ye, and P. Cheng, *Matching of water and temperature fields in proton exchange membrane fuel cells with non-uniform distributions.* International Journal of Hydrogen Energy, 2011. **36**(19): p. 12524-12537.
57. Wu, H., P. Berg, and X. Li, *Modeling of PEMFC Transients with Finite-Rate Phase-Transfer Processes.* Journal of The Electrochemical Society, 2010. **157**.
58. Shah, A.A., et al., *Transient non-isothermal model of a polymer electrolyte fuel cell.* Journal of Power Sources, 2007. **163**(2): p. 793-806.
59. Weber, A.Z. and J. Newman, *Transport in Polymer-Electrolyte Membranes I. Physical model.* Journal of The Electrochemical Society, 2003. **150**(7): p. A1008-A1015.

60. Weber, A.Z. and J. Newman, *Transport in Polymer-Electrolyte Membranes II. Mathematical model.* Journal of The Electrochemical Society, 2004. **151**(2): p. A311-A325.
61. Uchiyama, T., M. Kato, and T. Yoshida, *Buckling deformation of polymer electrolyte membrane and membrane electrode assembly under humidity cycles.* Journal of Power Sources, 2012. **206**: p. 37-46.
62. Kusoglu, A., et al., *Mechanical behavior of fuel cell membranes under humidity cycles and effect of swelling anisotropy on the fatigue stresses.* Journal of Power Sources, 2007. **170**(2): p. 345-358.
63. Silberstein, M.N. and M.C. Boyce, *Hygro-thermal mechanical behavior of Nafion during constrained swelling.* Journal of Power Sources, 2011. **196**(7): p. 3452-3460.
64. Ge, S., et al., *Absorption, Desorption, and Transport of Water in Polymer Electrolyte Membranes for Fuel Cells.* Journal of The Electrochemical Society, 2005. **152**: p. A1149.
65. Suzuki, T., K. Kudo, and Y. Morimoto, *Model for investigation of oxygen transport limitation in a polymer electrolyte fuel cell.* Journal of Power Sources, 2013. **222**: p. 379-389.
66. Nonoyama, N., et al., *Analysis of Oxygen-Transport Diffusion Resistance in Proton-Exchange-Membrane Fuel Cells.* Journal of The Electrochemical Society, 2011. **158**(4): p. B416.
67. Takamura, Y., et al., *Effects of Temperature and Relative Humidity on Oxygen Permeation in Nafion (R) and Sulfonated Poly(Arylene Ether Sulfone).* ECS Transactions, 2008. **16**.
68. Pasaogullari, U. and C.-Y. Wang, *Two-phase transport and the role of micro-porous layer in polymer electrolyte fuel cells.* Electrochimica Acta, 2004. **49**(25): p. 4359-4369.
69. Weng, D., et al., *Electro‐osmotic Drag Coefficient of Water and Methanol in Polymer Electrolytes at Elevated Temperatures.* Journal of The Electrochemical Society, 1996. **143**: p. 1260-1263.
70. Leverett, M.C., *Capillary Behavior in Porous Solids.* Transactions of the AIME, 1941. **142**(01): p. 152-169.
71. Udell, K., *Heat Transfer in Porous Media Considering Phase Change and Capillarity—The Heat Pipe Effect.* International Journal of Heat and Mass Transfer, 1985. **28**: p. 485-495.
72. Das, P.K., X. Li, and Z.S. Liu, *Analysis of liquid water transport in cathode catalyst layer of PEM fuel cells.* International Journal of Hydrogen Energy, 2010. **35**(6): p. 2403-2416.
73. Das, P.K., et al., *Effects of catalyst layer structure and wettability on liquid water transport in polymer electrolyte membrane fuel cell.* International Journal of Energy Research, 2011. **35**(15): p. 1325-1339.
74. Kumbur, E., K. Sharp, and M.M. Mench, *Validated Leverett Approach for Multiphase Flow in PEFC Diffusion Media.* Journal of The Electrochemical Society, 2007. **154**.
75. Das, P.K., et al., *Liquid-Water-Droplet Adhesion-Force Measurements on Fresh and Aged Fuel-Cell Gas-Diffusion Layers.* Journal of the Electrochemical Society, 2012. **159**(5): p. B489-B496.
76. Thumbarathy, D., et al., *Fabrication and Characterization of Tuneable Flow-Channel/Gas-Diffusion-Layer Interface for Polymer Electrolyte Fuel Cells.* Journal of Electrochemical Energy Conversion and Storage, February 2020. **17**(1): p. 011010.